Research Square

Preprints are preliminary reports that have not undergone peer review.
They should not be considered conclusive, used to inform clinical practice,
or referenced by the media as validated information.

A free-drifting wave buoy above the 2025 Mw 8.8 Kamchatka rupture

Gunther Kletetschka

gkletetschka@alaska.edu

University of Alaska Fairbanks, Geophysical Institute

Christopher Maio

University of Alaska Fairbanks

Article

Keywords: 2025 Kamchatka earthquake, Drifting wave buoy, Near-field tsunami, Detection limits, Multiple testing, Sofar Spotter

Posted Date: November 23rd, 2026

DOI: https://doi.org/10.21203/rs.3.rs-11528916/v1

License: This work is licensed under a Creative Commons Attribution 4.0 International License.
Read Full License

Additional Declarations: No competing interests reported.

A free-drifting wave buoy above the 2025 M_w 8.8 Kamchatka rupture

Gunther Kletetschka[1,2,*] & Christopher Maio[3]

[1]University of Alaska Fairbanks, Geophysical Institute, Fairbanks, Alaska, USA. [2]Charles University, Faculty of Science, Albertov 6, Prague, Czechia. [3]University of Alaska Fairbanks, Department of Geosciences, Fairbanks, Alaska, USA.

*email: gkletetschka@alaska.edu

ORCID:

Gunther Kletetschka https://orcid.org/0000-0002-0645-9037

Christopher Maio https://orcid.org/0000-0003-2993-7764

Abstract. On 29 July 2025, the magnitude 8.8 Kamchatka earthquake broke the fault beneath a drifting wave buoy. The buoy reported summary values of the waves and its position every 30 min, and sea-surface temperature and air pressure hourly. At the buoy, the U.S. Geological Survey's fault-slip model predicts about 10 cm of seafloor uplift, sea-level swings of about ±1 m and brief currents moving water 32–52 m between position fixes. Rising drift speed, 0.82 K sea-surface warming and less variation in wave height were within ordinary variability. Air pressure held steady from before the earthquake: a weather-related rise offset a daily fall. Tested alone, a 12-hour drift-speed change of about 0.2 m s^{-1}, or warming of about 1.2 K, would have been revealed only half the time. Two features remain unexplained. Drift speed jumped by 0.134 m s^{-1} after the earthquake, despite the modelled tsunami moving water roughly against the drift, and could reflect one 50–90 m position error. Mean wave period dipped in the 30-min records during which seismic waves from this and three other magnitude ≥ 7.4 earthquakes reached the buoy, with no plausible mechanism known. Neither feature establishes an earthquake effect. We identify measurements to test both.

Keywords. 2025 Kamchatka earthquake · Drifting wave buoy · Near-field tsunami · Detection limits · Multiple testing · Sofar Spotter

Introduction

On 29 July 2025, a magnitude (M_w) 8.8 earthquake [1] broke about 400–500 km of the fault where one tectonic plate slides beneath another, off south-eastern Kamchatka [2,3]. How far the fault moved near the trench, the deep trough where the plates meet, is disputed. Land data and sparse seafloor pressure measurements alone could not have revealed it [4]. Tsunami and satellite-positioning data (Global Navigation Satellite System, GNSS, which includes GPS) indicate 10–13 m [3], and satellite measurements of sea-surface height place the tsunami's generation within about 10 km of the trench [4]. But a model fitted to Deep-ocean Assessment and Reporting of Tsunamis (DART) records indicates little or no movement there [2]. On land, the tsunami reached at least 2–3 m above sea level along at least 550 km of the Kamchatka and northern Kuril coasts [5] (Methods).

Offshore, tsunamis are recorded by seafloor pressure gauges [6], including DART stations [7] and gauges cabled to shore above earthquake zones [8,9], and by anchored buoys with GPS [10–12]. More than 100 Sofar Spotter drifting wave buoys, which measure the motion of the sea surface using signals from navigation satellites, have reported in real time across the Pacific [13]. Every 30 min they usually transmit only their position, called a fix, and a record: a few summary values computed on board, such as wave height, period and direction, which leave out a tsunami's slow rise and fall [14,15]. We found no peer-reviewed report of a wave buoy recording the 2025 earthquake close to its source.

When the earthquake began, one such buoy, Spotter SPOT-31540C (Methods), was 52 km from the epicentre, in 2,671 m of water, about 90 km landward of the trench (Fig. 1). It lay above the rupture in the U.S. Geological Survey (USGS) fault-slip model, which estimates how far, in which direction and when each patch of the fault moved. We analyse only its records of 1 July–2 December 2025 (the data series), apart from a later test on its other records (Supplementary Methods S1.11).

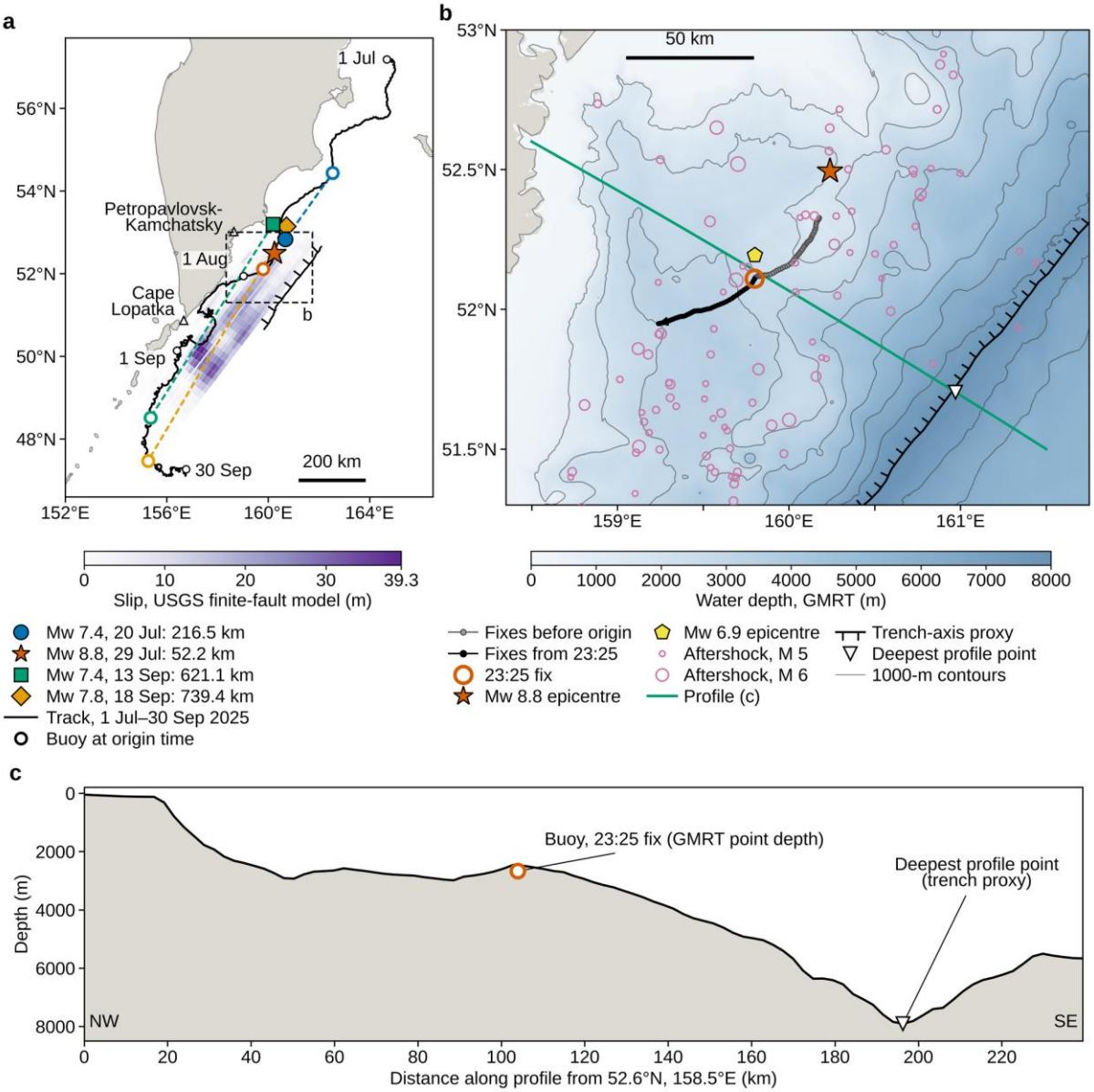


Figure 1. *Where the buoy, Spotter SPOT-31540C, was during the four M ≥ 7.4 earthquakes of July–September 2025.* ***a*** *Buoy track, 1 July–30 September (small circles: first satellite position fix on each labelled date). Epicentres (all magnitudes* M_{ww}*, the W-phase moment magnitude; Table 1) are joined by dashed lines to the buoy position interpolated to each origin time (when the earthquake began), with epicentral distances. Purple: fault movement (slip) in the USGS fault-slip (finite-fault) model us6000qw60, model 1, version 5 (maximum 39.3 m). Triangles: localities; dashed box: area of b.* ***b*** *Close-up of the dashed box, shaded by water depth from the Global Multi-Resolution Topography (GMRT) compilation, version 4.5.0. Trench-axis proxy (also in a): estimated trench line, where two tectonic plates meet, through the deepest grid values on lines drawn across the trench, spaced along the fault's 217° direction (strike). Fixes, 30 min apart, from 00:25 UTC on 29 July to 23:55 UTC on 30*

July (arrowhead: last fix). Water depth: 1,881–3,420 m within 12 h of the M_w 8.8 origin time. The 23:25 fix (vermillion ring) is stamped 7.5 s after the origin time. The M_w 6.9 (00:09:59.0 UTC), the largest aftershock in the first day, was 10.6 km (epicentral distance) from the buoy. Aftershocks: the 129 other M ≥ 5 earthquakes in the Advanced National Seismic System Comprehensive Catalog (ComCat) within 300 km of 52.5°N, 160.2°E, from the origin time to 00:00 UTC on 31 July (91 in the map). Most have body-wave magnitudes (m_b); circle diameter: 2.5 pt at M 5, plus 3 pt per magnitude unit. ***c*** *GMRT depth along the profile (green line in b). The 23:25 fix, 2.8 km off the profile, is projected onto it and drawn at the depth at the fix, 2,671 m (profile depth 2,469 m). The profile's deepest point, 7,909 m, is 92.4 km seaward of the fix. Vertical scale exaggerated 7.0 times. Map axes are longitude and latitude scaled to each panel's mid-latitude, so the scale bar in a is correct at 47°N. Sources: USGS [43,44]; Ryan et al. [46]; Natural Earth [66]. Drawn with Matplotlib 3.11.2 [68].*

Drift speed, the buoy's speed between consecutive fixes, mostly reflects the near-surface current. After the M_w 8.8 earthquake (Fig. 2), it jumped by +0.134 m s^{-1} from the 30 min in which the earthquake began to the next (the drift-speed step). Within hours it had roughly doubled. Sea-surface temperature (SST) rose by about 0.8 K. The mean wave period, a typical period of the waves, dipped in the record during which seismic waves (ground vibrations) reached the buoy (the wave-period dip). Later inspection found such a dip at the three other earthquakes of magnitude M ≥ 7.4 in July–September 2025, 216–739 km from the buoy.

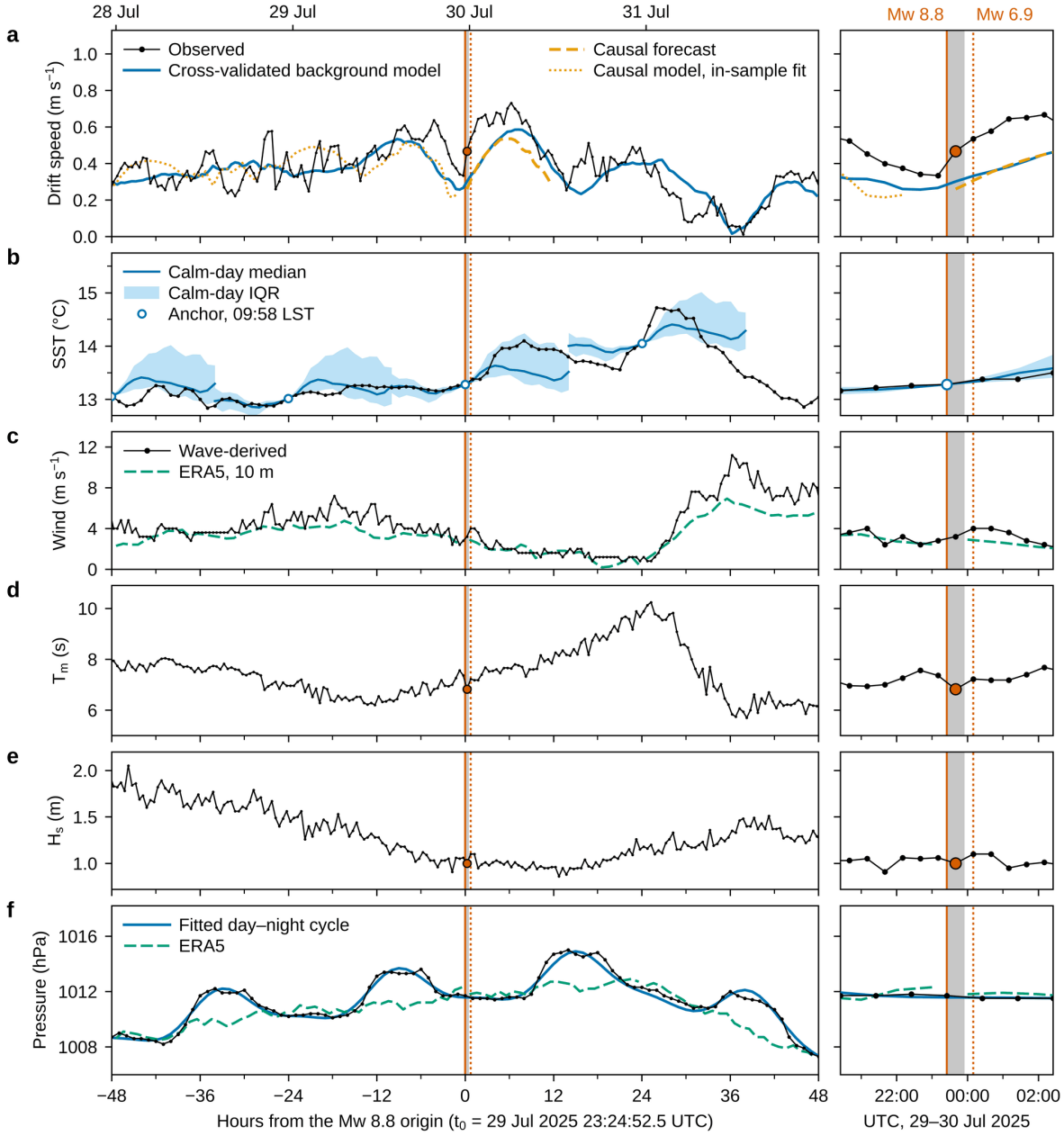


Figure 2. *The buoy's data around the M_w 8.8 earthquake. Left: ±48 h, in hours from the origin time t_0 (start of the earthquake); right: ±3 h, in UTC, same vertical scale. Vermillion solid and dotted lines: t_0 and the M_w 6.9 of 00:09:59.0 UTC, the largest aftershock in the first day; grey shading: the arrival record (time stamp 23:55), measured while seismic waves (ground vibrations) reached the buoy.* ***a*** *Drift speed between position fixes 30 min apart, at mid-interval. Blue: the preferred (cross-validated) background model of ordinary drift (Methods), fitted to 20 July–8 August, leaving out 1 h before to 12 h after each of the four $M \geq 7.4$ origin times, so in the left-out hours it is a prediction. Orange: a forecast fitted only to earlier data, $t_0 - 3$ d to $t_0 - 1$ h, and its fit to those data (in-sample fit). Vermillion dots: the*

first interval after t_0 (23:25–23:55 UTC), whose speed jumped (the drift-speed step). ***b*** *Hourly sea-surface temperature (SST), with the median and interquartile range of its change from 09:58 local apparent solar time (LST) on the 16 other calm (weak-wind) days of July–September, anchored at 09:58 each day.* ***c*** *Wind: wave-derived (inferred from the waves) and from ERA5, a global hourly reconstruction of past weather, at 10 m height (grid point nearest the buoy's daily-mean position, changed at 00:00 UTC).* ***d*** *Mean wave period T_m and* ***e*** *significant wave height H_s, standard measures of wave period and height from motion within the buoy's frequency band, which excludes tsunamis. Vermillion dots: the arrival record; in d, its low T_m is the wave-period dip.* ***f*** *Hourly air pressure (hectopascals, hPa), with ERA5 mean sea-level pressure and the fitted day–night cycle: 24-h running mean plus daily and twice-daily cycles (S_1, S_2). Departures from the cycle: +0.13 and −0.06 hPa at 23:25 and 00:25; standard deviation 0.31 hPa within ±48 h. The 13 consecutive hourly readings of 20:25–08:25 UTC stayed within 1,011.4–1,011.8 hPa. Statistics: Table 2 and Supplementary Table S12. Sources: Copernicus Climate Change Service [61]; Hersbach et al. [62]. Drawn with Matplotlib 3.11.2 [68].*

Features found by inspection call for caution: claimed warning signals before earthquakes have generally failed scrutiny [16], partly when the choices made in finding them were allowed for [17]. Physicists call this the look-elsewhere effect [18]: the more statistics one examines, the more likely one of them looks unusual by chance. We therefore predict, from the fault-slip model, how the seafloor and sea moved at the buoy, establish what the summary values can capture, test each feature against other times in the buoy's data, allowing for every statistic we recorded, and identify measurements for future tests. Two features remain unexplained: the drift-speed step and the wave-period dip.

Results

All times are Coordinated Universal Time (UTC). The M_w 8.8 began at 23:24:52.5 on 29 July (the origin time), mid-morning in local solar time. Time stamps of records, and labels of drift intervals between consecutive fixes, mark the end of their 30 min. An earthquake's arrival record is the record during which its seismic waves reached the buoy (Table 1). Unless stated, each p is the fraction of all other times of the data series away from earthquakes at which the statistic was at least as extreme as at the earthquake, in the direction tested (one-sided; Methods). These comparison times are assumed to show what happens without an earthquake.

The family-wise p allows for the look-elsewhere effect: it is the fraction of comparison times, each treated like the earthquake, at which the smallest p in a group of statistics was at least as small as the p being judged. It counts only the recorded search: the statistics and analysis choices we evaluated and recorded. Every family-wise p is therefore a lower bound: the evidence may be weaker than it suggests. A feature survives correction for the recorded search only if its family-wise p over all recorded statistics is below 0.05, against comparisons that allow for any day–night cycle (Methods). A detection would also require (i) a statistic fixed in advance, or replication in independent data, and (ii) a physical mechanism that predicts its sign and approximate size. Table 2 lists the main tests.

What the fault-slip model predicts and what the buoy could measure

The buoy's 30-min data could reveal none of the seafloor uplift, sea-level swings and currents the model predicts. The buoy lies 0.57–0.58 km from the model's boundary between seafloor that rose (uplift) and seafloor that sank (subsidence), on the uplift side (Fig. 3a).

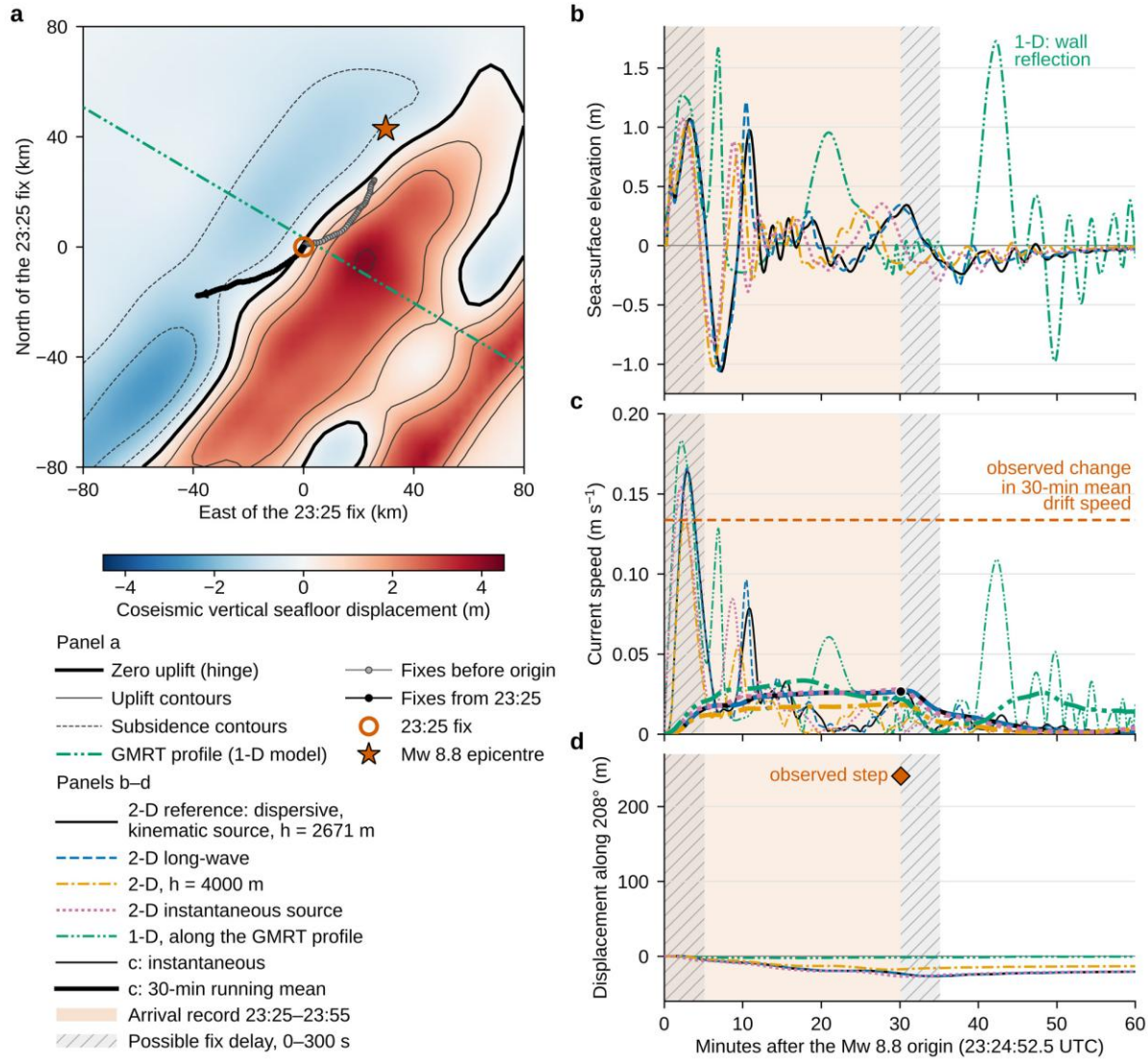


Figure 3. *Seafloor movement and tsunami at the buoy predicted from the USGS fault-slip model of the M_w 8.8 (Methods).* ***a*** *Vertical seafloor displacement Uz [47] during the earthquake (red: uplift; blue: subsidence) within ±80 km of the 23:25 fix, on the 4-km grid of the reference model (−2.6 to +4.1 m; colour scale unsaturated); fixes as in Fig. 1b. At the fix Uz is +0.10 m, 0.57–0.58 km from the hinge line between uplift and subsidence. Smoothed by the water above (1/cosh(kh) filter [48]; k, wavenumber; h, water depth), the initial sea-surface rise η_0 is +0.14 m.* ***b*** *Sea-surface elevation η: η_0 is small, but sea level swings by about ±1 m within 7 min.* ***c*** *Tsunami current speed: instantaneous (thin) and of the velocity averaged over the preceding 30 min (thick; peaks 0.018–0.028 m s^{-1} in the two-dimensional (2-D) runs, 0.033 m s^{-1} in the profile-only (1-D) model). Black dot: reference-run mean over 23:25–23:55 (0.027 m s^{-1}). Dashed line: observed drift-speed step (+0.134 m s^{-1}).* ***d*** *Tsunami water movement (how far currents carry the water and a floating buoy) since the 23:25 fix*

along the drift direction after the step (208°). Diamond: the extra movement of the buoy implied by the step (+241 m) at the 23:55 fix, where the 2-D runs shown give −17 to −27 m (the tsunami's contribution to the step over the hatched fix delays: −5 to −37 m; Results). The 1-D model's profile runs almost perpendicular to 208°, so its curve is near zero. Runs: implementation I1, the reference tsunami model (Supplementary Table S8); late 1-D peaks are reflections from the model's landward wall (Supplementary Methods S1.15). Hatching: possible fix delays (0–300 s). Predictions are unscaled and probably overestimates: the fault-slip model over-predicts the first crest at distant tsunami station DART 21416 about 1.5–2.2-fold (Supplementary Fig. S12). Observed values, from fixes 30 min apart, are not comparable with instantaneous values: compare the dashed line only with the thick lines in c, and the diamond only with values at the 23:55 fix. Sources: USGS [43,44]; Ryan et al. [46]. Drawn with Matplotlib 3.11.2 [68].

The model raises the seafloor at the buoy by 0.10 m; versions with other fault geometries or depths all give uplift (+0.03 to +0.94 m; Methods). Even so, with large fault patches and no offshore data, the model cannot tell whether the seafloor there rose or sank.

In the tsunami model (Methods), waves from nearby uplift and subsidence raise sea level at the buoy to +1.07 m after 3 min and lower it to −1.06 m after 7 min (Fig. 3b). Its brief currents, peaking at 0.12–0.18 m s^{-1} (Fig. 3c), carry the water, and a buoy in it, only 32–52 m between the 23:25 and 23:55 fixes (Supplementary Table S1). Within 2 h no water moves more than 60 m, so the tsunami changes the buoy's velocity over any drift interval by at most 0.034 m s^{-1} (Supplementary Note S2.8). These values probably overestimate the motion: at a distant DART station the fault-slip model over-predicts the first tsunami crest about 1.5–2.2-fold (Methods), a ratio not tested this close to the source.

The buoy computes its summary values from a wave spectrum, a breakdown of a record's sea-surface motion (its energy) by frequency; apparently, no spectra were transmitted (Methods). As far as we can tell, the summary values count only motion within a frequency band of about 0.03–0.8 hertz (Hz, cycles per second), whose upper limit in 2025 is undocumented (Methods). The significant wave height, H_s, a standard measure of wave height, is four times the standard deviation of sea-surface height within the band. The mean wave period, T_m, is the inverse of the average frequency of the motion, each frequency weighted by its energy. The tsunami, with periods of about 8–128 min [19], is far too slow for the band. Motion inside the

band, such as sound waves trapped in the water column, would enter the summary values (Methods).

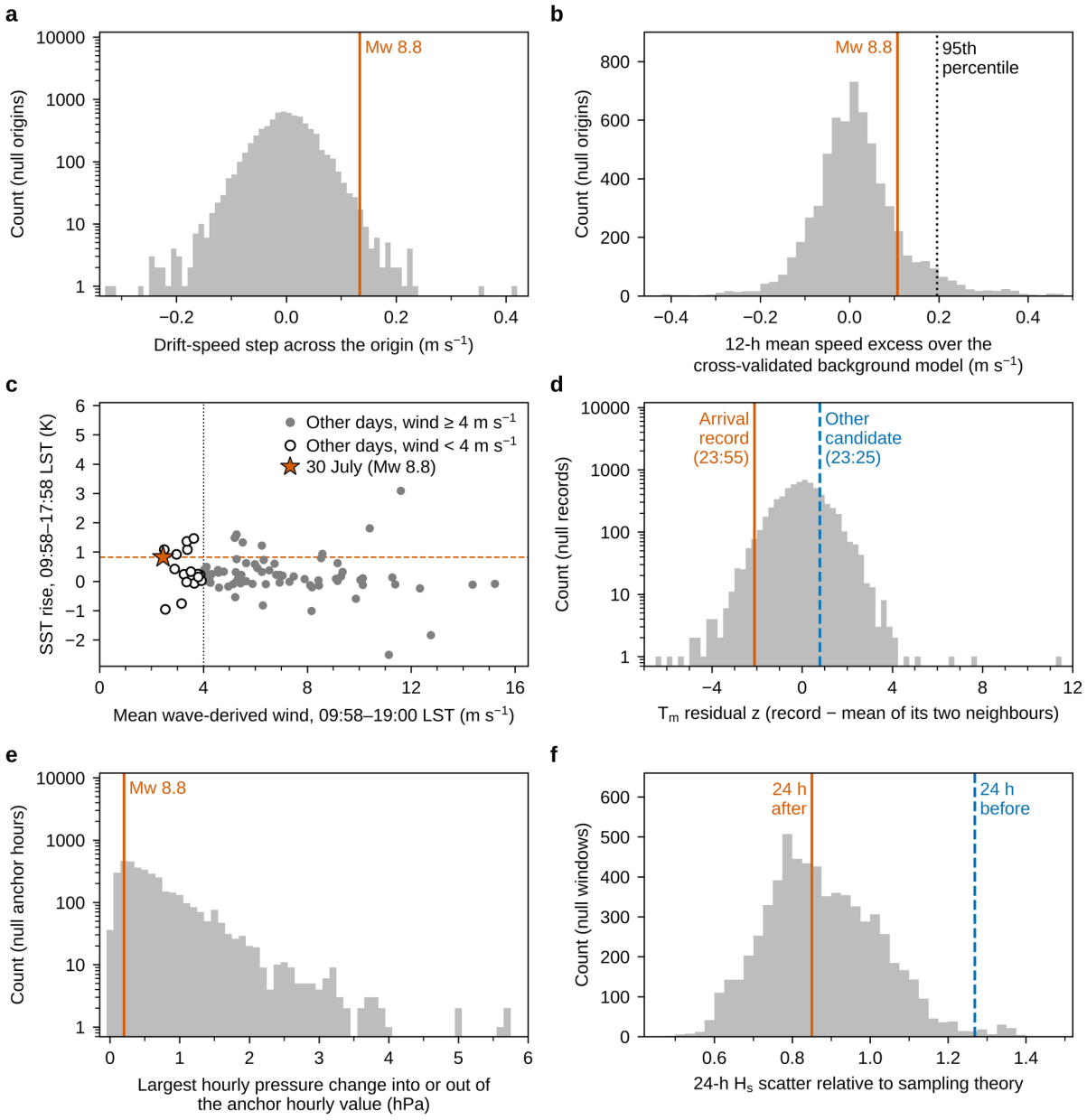
The rise in drift speed after the earthquake

The unexplained part of the rise depends on how ordinary drift is modelled; no drift statistic survives correction. Drift speed fell to 0.33 m s^{-1} at 23:25, then rose to 0.73 m s^{-1} at 05:55 on 30 July (Fig. 2a; Supplementary Note S2.1).

Drift speed rises and falls with clockwise rotations of the upper-ocean current, at a period close to one set by the Earth's rotation and latitude, usually started by earlier, on-and-off winds [20]. But a rotation as strong as the one before the earthquake could supply only part of the rise within 6 h, unless it grew (Supplementary Note S2.1; Supplementary Fig. S5).

Wind did not drive the rest. The wave-derived wind, which the buoy infers from the waves rather than measures, was only 2.0–4.4 m s^{-1} around the earthquake (Fig. 2c; Methods). Even so weak a wind can drive a brief daytime surge of current in a thin, sun-warmed surface layer [21]. But in ERA5, a global, hourly reconstruction of past weather (Methods), the wind blew across or against the drift (Supplementary Note S2.1).

Background models are statistical models of ordinary drift, fitted without the hours around the four $M \geq 7.4$ earthquakes (Methods). The preferred one, which best predicted drift left out of its fit at many other times (cross-validation), reproduces most of the rise (Fig. 2a). Its 12-h excess, observed minus predicted mean drift speed over the 12 h after the earthquake, is +0.107 m s^{-1} ($p = 0.14$; Fig. 4b; Supplementary Note S2.1).



205

206 ***Figure 4.*** *M_w 8.8 statistics (vermillion) against their comparison values (grey; 'null' on the*
207 *axes). Comparison values are the same statistic at times away from earthquakes, 1 July–2*
208 *December 2025 unless stated. p: fraction of comparison values at least as extreme, in the*
209 *direction tested (one-sided). Histograms show all values; a, d and e have logarithmic counts.*
210 ***a*** *Drift-speed step: change in drift speed into the first interval between fixes after the origin*
211 *time (start of the earthquake; 23:25–23:55). Comparison: 6,695 times more than 24 h from*
212 *the four M ≥ 7.4 origin times; p = 0.0072.* ***b*** *12-h excess of mean drift speed over the*
213 *preferred (cross-validated) background model of ordinary drift, refitted at each comparison*
214 *time. Comparison: 6,376 times at least 24 h from the four origin times; p = 0.14.* ***c*** *Sea-*
215 *surface temperature (SST) rise 09:58–17:58 local apparent solar time (LST) plotted against*

mean wave-derived wind 09:58–19:00 LST, not a daily mean. Comparison: the 88 other July–September days, 16 calm (wind < 4 m s⁻¹); p ≈ 0.35 (calm) and 0.16 (all). ***d*** *Residual z of mean wave period T_m: a record's departure from the mean of its two neighbouring records, in units of the typical departure nearby in time (Methods). Comparison: 6,442 records more than 12 h from all 31 M ≥ 6 earthquakes (Methods); arrival record (during which seismic waves reached the buoy), p = 0.027. The other candidate arrival record (blue dashed line; time stamp 23:25) is positive because the low arrival record is one of its neighbours.* ***e*** *Largest change into or out of an hourly air-pressure reading whose neighbours lie 1 h away (M_w 8.8: the 23:25 reading). Comparison: 3,568 readings more than 12 h from the four origin times; p = 0.91.* ***f*** *24-h wave-height scatter after and before the origin time: variation of significant wave height H_s around its running median, relative to sampling error alone (which would give 1). Comparison: 6,505 windows centred more than 48 h from the four origin times. The tested change between the two (p = 0.034) is not drawn. Plotted with Matplotlib 3.11.2 [68].*

A background model with a straight-line trend, specified first, leaves a 12-h excess of +0.31 m s⁻¹ (p = 0.04; Supplementary Table S3). Corrected only for the choice among background models, its family-wise p is 0.049–0.11. Over all recorded statistics, no drift statistic has a family-wise p below 0.16 (Supplementary Table S7).

The drift-speed step just after the earthquake

The drift-speed step does not survive correction; the tsunami cannot explain it, nor is wind its main cause. Speed rose by 0.134 m s⁻¹, from 0.333 m s⁻¹ in the drift interval ending 23:25, which contains the origin time, to 0.467 m s⁻¹ in the next. The step's uncorrected p (before allowing for other statistics) is 0.0072 (Fig. 4a). In the 24-feature search, a screen of candidate features (Methods), its family-wise p is 0.13 (rise only) to 0.24 (either direction).

We also tested the step together with the 6-h rise in speed after it, a combination defined after inspection (Methods; Supplementary Fig. S11). Among the 24 features plus this combination, its family-wise p, 0.036, is therefore a lower bound. The deciding test, over all 351 statistics recorded at the M_w 8.8, gives a family-wise p of 0.47–0.48 for the step and 0.16 for the combination, so neither survives correction (Supplementary Note S2.7).

The step needs +241 m of extra movement of the buoy along the drift (Fig. 3d), at least 4.0 times the modelled tsunami's largest movement of water within 2 h (Methods; Supplementary

Fig. S2). If the unknown delay between a record's time stamp and its fix is 0–300 s, the modelled tsunami lowers the step by 5–37 m of such movement (Supplementary Note S2.8). With no delay, the water's movement between the two fixes points 114–145° from the drift direction, only roughly backwards (Supplementary Fig. S4), but its part along the drift is backwards for every model and delay tested (Methods).

Even with a generously strong response of drift to wind, the wind change adds at most 0.015–0.04 m s^{-1} to the step, depending on the wind estimate (Supplementary Note S2.1).

A single displaced fix could produce the step: a 23:25 fix lying 53–88 m back along the drift, or taken 2–4 min early relative to neighbours, would make the interval ending 23:25 look too slow and the next too fast, leaving later intervals unchanged. The 23:25 fix does lie about that far from smooth paths through neighbouring fixes, almost all of it back along the drift. Such departures are uncommon but not rare: 3.2% of fixes lie at least as far back (Supplementary Fig. S4; Supplementary Table S12).

Mean wave period and wave height: the wave-period dip

In the arrival records of all four M ≥ 7.4 earthquakes, T_m was 3–12% below the mean of the two neighbouring records (Fig. 5a), with p = 0.077, 0.027, 0.0028 and 0.0096 in date order (Fig. 5c). This wave-period dip survives correction but is not a detection (Discussion). At the M_w 8.8, the residual z (this departure divided by its typical size nearby; Methods) was −2.11 (p = 0.027; Figs. 2d, 4d). Because the time-stamp convention was checked only later, the preceding record was also a candidate arrival record (Methods). Allowing for either record and either sign of departure raises the corrected p to 0.098. From about 13 h before the earthquake, T_m rose by about 3 s, reflecting swell (long-period waves from a distant storm) [22] and fading short waves raised by the local wind (Supplementary Note S2.5; Supplementary Fig. S9).

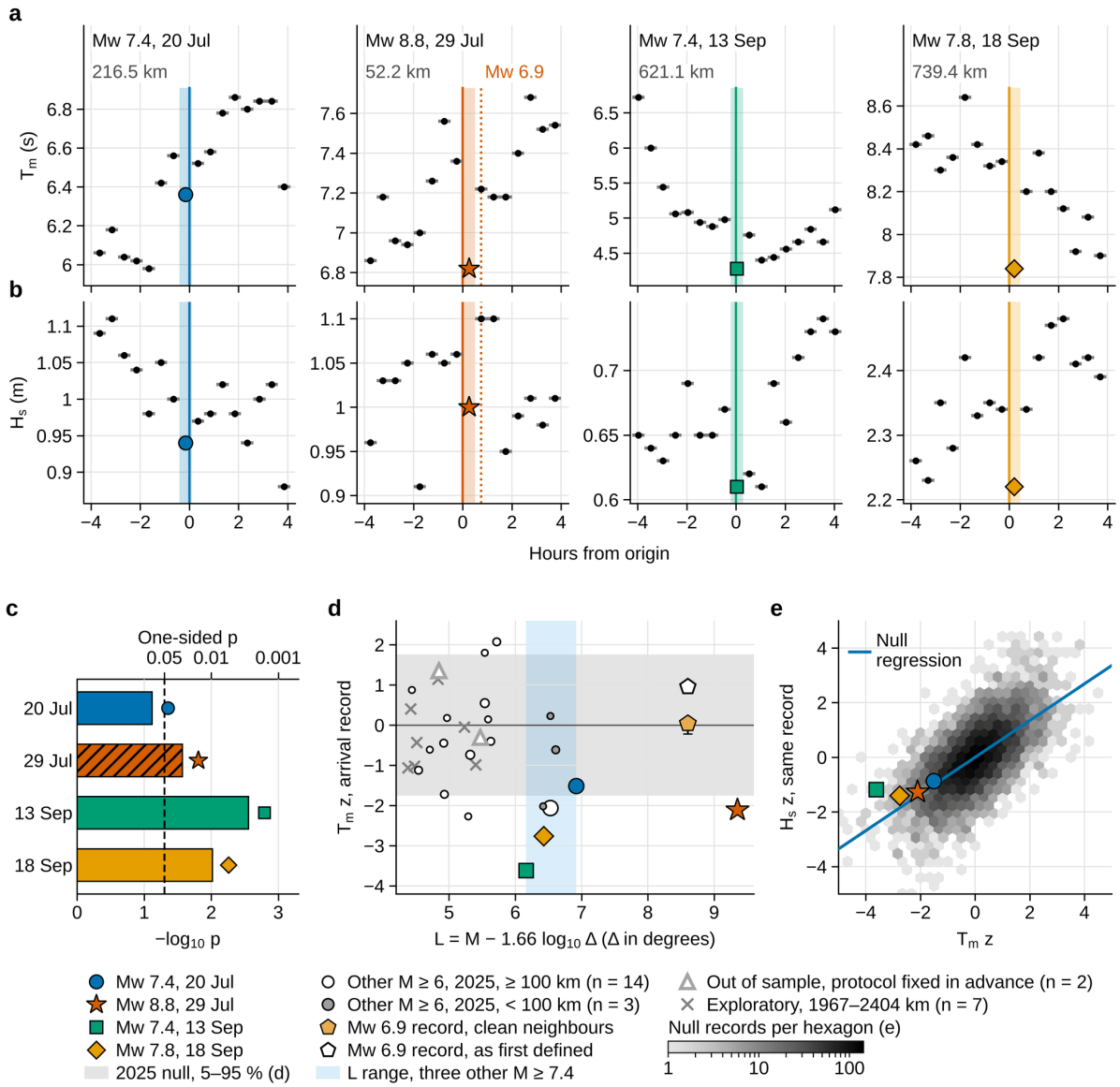


Figure 5. *The wave-period dip and further tests.* ***a*** *Mean wave period T_m and* ***b*** *significant wave height H_s within ±4.3 h of the four M ≥ 7.4 earthquakes of 2025 (all M_{ww}, the W-phase moment magnitude; Table 1; labels: epicentral distance). Grey bars: measurement period of each record. Shading and large symbol: the arrival record (first record time-stamped at or after origin time + 60 s), during which seismic waves reached the buoy; its low T_m is the dip. Solid line: origin time; dotted line: the M_w 6.9, the first day's largest aftershock.* ***c*** *One-sided p of each arrival record's T_m z (departure from neighbouring records) against the comparison values (null) of Fig. 4d, plotted as $-\log_{10} p$ (top axis: p): 0.077, 0.027, 0.0028 and 0.0096. Hatched: the M_w 8.8, at which the pattern was noticed; dashed line: p = 0.05. The dip survives correction for the recorded search but is not a detection, which also needs a statistic fixed in advance, or replication in independent data, and a physical mechanism that predicts*

its sign and approximate size (Table 2; Discussion). ***d*** *T_m z of each arrival record against the amplitude proxy $L = M - 1.66 \log_{10} \Delta$ (Δ, epicentral distance in degrees), a crude index for ranking earthquakes by the strength of their seismic surface waves (ground vibrations) at the buoy; not meaningful within about 100 km. Also shown (Supplementary Table S5): 17 other $M \geq 6$ earthquakes of 2025 (Methods; size grows with magnitude); the M_w 6.9 record as first defined and with neighbours outside the M_w 8.8 arrival record (mean and range of three such choices); the two earthquakes of the out-of-sample test (protocol fixed in advance); and seven exploratory $M \geq 6.5$ earthquakes too distant for the protocol. The last two groups use comparison values of 2 December 2025–11 October 2026 ($N = 9{,}905$).* ***e*** *H_s z against T_m z: comparison records of Fig. 4d (hexagons, logarithmic count; 12 with $|z| > 5$ off axes), their regression line (slope 0.67, $r = 0.66$) and the four arrival records. Drawn with Matplotlib 3.11.2 [68].*

Because the dip was noticed at the M_w 8.8, it is judged on the other three, whose p-values, combined by Fisher's method, give a Fisher p of 2.1×10^{-4}. This statistic was adopted after 105 wave statistics had been evaluated at all four (Supplementary Methods S1.10). In the main analysis, against random sets of three comparison times (Methods), the family-wise p is $3.3–7.5 \times 10^{-3}$ over these statistics and at most 1.6×10^{-2} including the other analyses, both below 0.05 (Supplementary Fig. S10; Supplementary Note S2.6).

The other $M \geq 6$ earthquakes of July–December 2025 with their own arrival records lean weakly towards a dip (uncorrected Fisher p = 0.052; Supplementary Note S2.6). The nearby M_w 6.9 aftershock's arrival record (Table 1) shows no dip (z = −0.2 to +0.2; Fig. 5d).

Table 1. *Earthquakes, buoy positions and distances, and arrival records (the 30-min records during which each earthquake's seismic waves reached the buoy). Times are UTC; origin times (when each earthquake began) are rounded to 0.1 s. Time stamps mark the end of each record's 30-min measurement period [41]; a fix is the satellite position sent with each record. Earthquake parameters are from the Advanced National Seismic System Comprehensive Catalog (ComCat) of the USGS [1,43]. Magnitudes are its preferred values: M_{ww}, the W-phase moment magnitude (from long-period seismic waves), for the five earthquakes listed; M_{ww} or body-wave magnitude m_b, as given, for the other $M \geq 6$ earthquakes (all earthquakes used are listed in Supplementary Table S5). A foreshock is a smaller earthquake that precedes a larger one in the same area. Epicentral distances are along the Earth's surface (on a sphere, R = 6,371 km), from the buoy position interpolated to the origin time. Hypocentral distances are straight lines through the Earth to the hypocentre, where the rupture began. Because the Earth is curved, straight down at a distant epicentre points partly towards the buoy, so beyond an epicentral distance of about $\sqrt{(hR)}$, with h the depth, hypocentral distances are shorter than epicentral ones (Supplementary Methods S1.9). P (compressional) and S (shear) waves travel through the Earth, and Rayleigh waves along its surface. Their arrival times are estimates that treat each earthquake as a single point, with speeds $v_P = 7$ and $v_S = 4$ km s^{-1} over the hypocentral distance and $v_R = 3.5$ km s^{-1} over the epicentral distance.*

Earthquake (ComCat id)	Origin time	M_w (M_{ww})	Epicentre (°N, °E), depth (km)	Buoy fix nearest the origin time: time stamp (°N, °E)	Epicentral / hypocentral distance (km)	P / S / Rayleigh arrival (s after origin time)	Arrival record: time stamp (30-min measurement period)	Other M ≥ 6 earthquakes in the arrival record
us7000qdyl	2025-07-20 06:49:04.3	7.4	52.830, 160.682, 34	06:55 (54.432, 162.544)	216.5 / 218.6	31 / 55 / 62	06:55 (06:25–06:55)	M 6.6 (M_{ww}) foreshock, 06:28:17.9 [b]
us6000qw60	2025-07-29 23:24:52.5	8.8	52.495, 160.240, 35	23:25 (52.110, 159.799)	52.2 / 62.7	9 / 16 / — [a]	23:55 (23:25–23:55)	M 6.3 23:30:03.0; M 6.1 23:30:44.6; M 6.0 23:36:01.3; M 6.0 23:37:34.4 (all m_b)
us6000qw6q (largest aftershock in the first day)	2025-07-30 00:09:59.0	6.9	52.195, 159.801, 37	23:55 (52.103, 159.794)	10.6 / 38.1 [c]	5 / 10 / —	00:25 (23:55–00:25)	M 6.2 (m_b), 00:16:06.5, 6.6 km from the buoy (epicentral)
us7000qvw5	2025-09-13 02:37:56.8	7.4	53.197, 160.190, 58	02:25 (48.514, 155.361)	621.1 / 620.7	89 / 155 / 177	02:55 (02:25–02:55)	none
us7000qx2g	2025-09-18 18:58:14.9	7.8	53.143, 160.721, 27	18:55 (47.472, 155.272)	739.4 / 737.9	105 / 184 / 211	19:25 (18:55–19:25)	none

[a] Approximate, because the rupture was hundreds of kilometres long and the buoy lay above it; at this distance Rayleigh waves cannot be separated from S waves. From the ComCat hypocentre, 35 km deep, the first P waves reached the sea surface at the buoy at 23:25:01.9–23:25:04.7. From the shallower hypocentre of the USGS fault-slip model, 17 km deep,

they arrived about 1 s sooner after the origin time. At the water depth of the 23:25 fix (2,671 m, from the Global Multi-Resolution Topography compilation, GMRT), tsunami waves (long waves) travel 52 km in 5.4 min.

[b] The next record (time stamp 07:25, measured 06:55–07:25), one of the two neighbouring records used for this earthquake's residual z of T_m, is the record during which an M 6.6 and an M 6.5 aftershock occurred (M_{ww}; 07:07:42.6 and 07:23:02.1).

[c] 10.2 / 38.0 km from the 23:55 fix. Rayleigh arrival times are not meaningful at this distance. The standard residual z of T_m for this record uses the M_w 8.8 arrival record (time stamp 23:55) as a neighbour, so the Results section uses other neighbouring records instead.

Ordinary causes cannot be excluded. On 13 September the dip coincided with a switch of the most energetic waves between two swells. Comparison records preceded by a similar mix of wave periods are too few to test whether this coincidence explains the dip (Supplementary Methods S1.10). ERA5 shows no wind shift or weather front at any arrival record, but the wave-derived wind cannot test for a short gust, which would add local wind waves and lower T_m (Supplementary Methods S1.13; Supplementary Fig. S10). The other three tsunamis could not have reached the buoy within their arrival records (Methods).

H_s was also low in all four arrival records ($z = -0.87$ to -1.41; Fig. 5b), as expected: both come from the same 30 min of an irregular sea, so random errors tend to move them together. Added energy, extra sea-surface motion within the frequency band (for example from shaking, measured as variance in square metres), would instead raise H_s above the value T_m predicts. H_s exceeded that prediction at all four, but not beyond what chance would give (Fisher $p = 0.13$ without the M_w 8.8; Fig. 5e), so random error and added energy cannot be told apart.

Out-of-sample test. We tested the dip on wave data and earthquakes not examined when the protocol was written. The protocol, not registered with a third party, fixed the statistic, the rules for choosing earthquakes and data, and the decision rule (Methods). Two $M \geq 6.5$ earthquakes within 1,500 km qualified; neither showed a dip (Fisher $p = 0.72$; Supplementary Note S2.6). By the amplitude proxy L, a crude index of how strong seismic surface waves (ground vibrations along the Earth's surface) would be at the buoy (Methods), they were about 5 and 20 times weaker than the weakest of the other three $M \geq 7.4$ earthquakes (Fig. 5d). Power, the test's probability of giving Fisher $p \leq 0.05$, was 0.96 for the average dip at those three and 0.54 at the weaker end of that average's 95% confidence interval; choosing the statistic after inspection probably makes both sizes too large. For a dip weakened by those factors of about 5 and 20, the power was about 0.10 (Supplementary Methods S1.11). Under the protocol's decision rule, Fisher $p > 0.05$ with power ≥ 0.80 for the observed size means the dip fails. This is inconsistent with a dip of that size at every $M \geq 6.5$ earthquake within 1,500 km, but not with a smaller dip common to all. No large nearby earthquake was sampled, so a dip confined to such earthquakes is neither replicated nor refuted.

Sea-surface temperature, air pressure, wave-height scatter and combined tests

Allowing for the day–night cycle, daytime heating and the recorded search, nothing below points to the earthquake.

SST. From the earthquake to late afternoon, SST rose by 0.82 K (Fig. 2b), which is ordinary against the 16 other calm days (mean wind below 4 m s^{-1}; $p \approx 0.35$) and the 88 other July–September days ($p = 0.16$; Fig. 4c). Calculations of daytime warming [21,23–25] predict less warming from morning minimum to afternoon maximum than observed. This excess, the largest of six complete days around the earthquake, is within the range expected, 95% of the time, from the other five (Supplementary Note S2.2; Supplementary Fig. S6).

Air pressure. Pressure stayed within 1,011.4–1,011.8 hectopascals (hPa) for 13 hourly readings spanning the earthquake (the flat stretch; Fig. 2f); its largest hourly change across the earthquake was 0.2 hPa ($p = 0.82$–0.92; Fig. 4e). The readings have a large day–night cycle, absent from ERA5 and probably an instrument effect (Methods; Supplementary Note S2.3; Supplementary Fig. S7).

Table 2. *The main tests at the M_w 8.8 earthquake, and of the wave-period dip (low mean wave period T_m in the arrival record) at the four M ≥ 7.4 earthquakes. Full version: Supplementary Table S12.*

Quantity: statistic	Observed	Uncorrected p	Family-wise p (corrected for the recorded search)	Assessment
Drift: the drift-speed step, 23:25–23:55 vs 22:55–23:25	+0.134 m s^{-1}	0.0072 (N = 6,695); 0.46–0.55 at the other three M ≥ 7.4 earthquakes	0.13, 24-feature search; 0.47–0.48, all 351 statistics recorded at the M_w 8.8	Does not survive correction; modelled tsunami contribution roughly against the drift and ≥ 4.0 times too small; could be a displaced 23:25 fix
Drift: change in velocity (speed and direction), same intervals	0.138 m s^{-1} toward 196°	0.094 (N = 6,748)	—	Ordinary; nearly along the drift
Drift: 12-h excess, preferred (cross-validated) background model	+0.107 m s^{-1}	0.14 (N = 6,376)	0.099, 4 background models × 3 statistics	No attributable signal
Drift: 12-h excess, causal forecast (fitted only to earlier data)	+0.161 m s^{-1}	0.12 (N = 6,630)	Included in the 0.099 above	Rise predictable from data before the earthquake
Drift: largest rise within 6 h	+0.37 m s^{-1}	0.071 (N = 6,886)	0.17, 3 statistics at 6 h	Not significant
SST: rise 09:58–17:58 LST	+0.82 K	0.35 (16 other calm days); 0.16 (88 other July–September days)	0.65 / 0.34 (same comparison days), 9 statistics	No signal
T_m: M_w 8.8 arrival record	z = −2.11 (6.82 s)	0.027 (N = 6,442)	0.098, either candidate record and either sign; 0.49, 7 wave variables × 2 candidate records	Not significant alone
T_m: arrival record, four M ≥ 7.4 earthquakes (the wave-period dip)	z = −1.52 / −2.11 / −3.62 / −2.76	0.077 / 0.027 / 0.0028 / 0.0096; Fisher p (three earthquakes other than the M_w 8.8) 2.1 × 10^{-4}; 1.3 × 10^{-4} to about 3 × 10^{-2} across definitions of z	Three earthquakes other than the M_w 8.8, for the smallest p of the group: 3.3 × 10^{-3} over 105 statistics of the wave records, 6.6–7.4 × 10^{-3} over the 273–351 statistics of the three-earthquake search, all recorded before adoption; for the adopted statistic itself, over the same groups: 7.5 × 10^{-3} and 1.5–1.6 × 10^{-2}	Survives correction for the recorded search; not a detection (statistic chosen after inspection; no plausible mechanism; not replicated)
T_m: other M ≥ 6 earthquakes	17 records for which z could be computed	Fisher p 0.052	—	Weak, same direction
T_m: arrival record of the M_w 6.9 aftershock	z = −0.2 to +0.2	—	—	No dip
T_m: out-of-sample test	2 earthquakes; z = −0.31 / +1.35	0.38 / 0.91; Fisher p 0.72. Comparison times: Supplementary Methods S1.11 (N = 9,905)	—	Protocol verdict: fails (uniform effect); a dip limited to large nearby earthquakes not testable
H_s relative to that expected from T_m, four earthquakes	Residuals +0.15 / +0.15 / +1.25 / +0.45	Fisher p (three earthquakes other than the M_w 8.8) 0.13	—	Cannot separate linked random errors from added energy
Air pressure: largest hourly change across t_0	0.2 hPa	0.82–0.92 (all comparison sets tried)	—	No anomaly
Air pressure: buoy minus ERA5, day–night cycle removed	−0.23 / −0.31 / −0.07 hPa at 22:25 / 23:25 / 00:25	0.12–0.15 (23:25), 0.42–0.43 (00:25); one-sided, testing for low values	—	Ordinary; the departure began before t_0

Quantity: statistic	Observed	Uncorrected p	Family-wise p (corrected for the recorded search)	Assessment
Wave-height scatter: change after vs before (24 h)	3.4th percentile	0.034	0.19, 15 statistics	No signal (noisy preceding day)
Combined test: 23 features (Fisher's method)	X = 76.5	0.018 (all comparison times)	— (combined test)	Not specific to the origin time; inflated by selection
Humidity inside the housing: 1-h change spanning t_0	−4.0 percentage points	0.016 (comparison times at the same time of day)	0.015, 3 instrument readings (humidity, power, battery voltage; all 6,748 comparison times); 0.24, 24-feature search	Largest hourly fall in a daytime decline; probably thermal (warming of the housing)

p: one-sided, in the direction claimed, (k + 1)/(N + 1), where k of the N comparison times are at least as extreme; unless stated, these are all other eligible times of 1 July–2 December 2025 (Methods). Same time of day: within ±1 h of the earthquake's local mean solar time, which differs slightly from the local apparent solar time (LST) of the SST row (N = 563 of the 6,748 times of the 24-feature search). Uncorrected p: the statistic as defined, against its own comparison times. Family-wise p: corrected for all statistics of the named group (Methods; Supplementary Tables S6 and S7); a lower bound, because analysis choices that left no record cannot be counted. For the humidity it is slightly below the uncorrected p, because these coarsely stepped readings produce many ties (Supplementary Methods S1.12). Ranges span alternative comparison times, definitions, models or implementations, or other earthquakes. Bold: the two unexplained features (Supplementary Table S12 and the rest of the Supplementary Information call the wave-period dip the arrival-record T_m dip). Arrival record: the record during which an earthquake's seismic waves reached the buoy (Table 1); candidate records: the two that could have been chosen for the M_w 8.8 (Methods). z: a record's departure from the mean of its two neighbours, in units of the typical departure nearby in time. Wave-height scatter: the record-to-record variation of H_s around its running median. Three-earthquake search: the wave statistics and the statistics of the separate air-pressure, wave-height-scatter, SST and drift analyses, all counted in the search for the wave-period dip (Methods). Fisher p: the p-values of several earthquakes combined by Fisher's method; X, the Fisher statistic of the combined test. t_0, origin time of the M_w 8.8; T_m, mean wave period; H_s, significant wave height; SST, sea-surface temperature; ERA5, a global hourly reconstruction of past weather (Methods).

The flat stretch began 3 h before the earthquake, as a weather-related rise offset the cycle's daytime fall. Its narrow range is unusual against all comparison times ($p = 0.0003$; family-wise p over all recorded statistics 0.025), but these ignore the cycle and do not count. Against comparison times at about the same time of day, or with the cycle removed, p is 0.0024–0.14 and no such family-wise p is below 0.16 (Supplementary Table S7), so the flat stretch does not survive correction. With the cycle removed, the departure from ERA5 is ordinary at the earthquake and began before it (Table 2).

Wave-height scatter. This is the record-to-record variation of H_s around its running median over a few hours. Its apparent fall after the earthquake reflects an unusually noisy preceding day (98.7th percentile), not a quiet following day (46.6th; Fig. 4f; Supplementary Fig. S8). The change ($p = 0.034$) has a family-wise p of 0.19 (Supplementary Table S7).

Combined tests. Combining the p-values of 23 of the 24 candidate features (excluding the one added after inspection) tests whether they are unusual together. Against the same combination at the comparison times, p is 0.018, or 0.055 without the six features noticed by eye (Supplementary Methods S1.12). This is not specific to the earthquake: three other times within ±48 h give smaller values (Supplementary Fig. S11). Rises in drift speed and SST this large rarely coincide, but the pair was examined only because both were seen together (Supplementary Table S12).

Humidity. Humidity inside the sealed housing fell across the earthquake (uncorrected $p = 0.016$ against the same time of day; family-wise p 0.24 in the 24-feature search), probably because the housing warmed by day (Supplementary Note S2.7).

Detection limits: how large a change the data could reveal

Tested one statistic at a time, the data could reveal only changes larger than predicted. A detection limit (δ_{50}) is the smallest change a statistic would flag as unusual (one-sided $p \leq 0.05$) half the time (Methods; Supplementary Table S1; Supplementary Fig. S3); a change sought among several would have to be larger.

Drift. The 12-h excess and the drift-speed step have detection limits of 0.19–0.25 m s^{-1} (across background models) and 0.08 m s^{-1}. The observed step exceeds its limit but does not survive correction. The modelled tsunami would lower the step, cutting the probability of flagging it as a rise to 0.02–0.04, below the 0.05 expected with no signal.

SST. The limit is 1.33 K against all other July–September days; with only 16 calm days no result can reach $p \leq 0.05$, so other criteria give 1.13–1.21 K (Supplementary Methods S1.3).

Heating by the earthquake, at most 0.17 K even under a deliberately extreme assumption, is about 7–8 times smaller (Supplementary Fig. S2).

Air pressure. Earthquakes set off pressure waves in the air, recorded by sensitive barometers [26–29]. If each hourly reading is a 1-h mean, which is not documented, physically based scenarios for these waves lie 14–260 times below the limits (Methods; Supplementary Fig. S2).

Added wave energy. Energy added by shaking to the M_w 8.8 arrival record has a detection limit of 0.014–0.016 m². That record's H_s, near the value its T_m predicts, excludes additions above 0.0088 m² (one-sided 95% level) whatever their frequencies, and above 0.0017–0.0034 m² at 0.3–0.5 Hz (Supplementary Note S2.4). Both limits assume that onboard processing left the record unaltered and that the buoy's satellite-derived motion stayed valid during the shaking, which we cannot check.

Discussion

The buoy lay above the M_w 8.8 rupture, yet its 30-min data show nothing traceable to the earthquake or the tsunami, which was strong on the nearby coast [5]. This absence reflects the data's limits, as the USGS fault-slip model and the buoy's design predict (Fig. 3). Every predicted signal lies below the change that one statistic, tested alone, would flag half the time; the modelled tsunami's effect on drift speed lies about 2.4 times below it (Results; Supplementary Table S1). Ordinary processes explain every unusual feature found by eye except the drift-speed step and the wave-period dip.

The drift-speed step does not survive correction, so chance cannot be excluded; it is not evidence of an earthquake effect. The tsunami is ruled out as its cause, and the wind as the main cause (Results). Unrelated ocean processes are plausible over the sloping seafloor, where large rotating currents can alter the upper-ocean current's clockwise rotations [30]. The simplest remaining explanation, one displaced 23:25 fix, cannot be told apart from a lasting change in velocity or fix timing (Supplementary Note S2.1). The fix, stamped 7.5 s after the origin time, may have been taken during the shaking, whose effect on fixes is unknown. If, as we assume (Methods), one GNSS receiver provides positions and wave measurements, a disturbance during the shaking could affect both unexplained features, which at the M_w 8.8 are not independent evidence.

The wave-period dip survives correction but is not a detection (Results): found and judged in the same data, it meets neither condition (i) nor (ii). Its statistic was chosen after all four

earthquakes were inspected, and it has not been replicated: it failed the out-of-sample test, which sampled no large nearby earthquake (Results). Its three-earthquake Fisher p depends on how the departure from neighbouring records is defined (Supplementary Table S6; Table 2) and on which record is taken as the arrival record. Three earthquakes give little protection against coincidences that the comparison times do not represent, such as the 13 September switch between swells or a change in the waves too local for ERA5 to show.

As for condition (ii), no mechanism of the right size at the sea surface is apparent for all four earthquakes. Seismic surface waves do move the ocean [31] (Supplementary Methods S1.2), but added energy lowers T_m only if it oscillates more rapidly, on average, than the waves already present. For added energy at 0.3–0.5 Hz, the dips 621 and 739 km from the epicentres would need up-and-down sea-surface speeds of at least 0.15–0.23 m s^{-1}, as a root-mean-square over the record (Supplementary Table S4). That is a third to a half of 0.48 m s^{-1}, the largest horizontal ground speed in the USGS map of estimated shaking for the M_w 8.8, which gives neither its location nor its direction [32]. Shaking that far from M_w 7.4–7.8 earthquakes is probably far weaker, although we have not estimated it there or at 216 km. The required motion is largest at the most distant earthquakes, and the nearby M_w 6.9 aftershock shows no dip (Fig. 5d): the reverse of what one would expect if stronger shaking caused larger dips.

Taken alone, the dip at the M_w 8.8, unlike the four-earthquake pattern, does have a possible mechanism. Ships at sea feel strong shaking during earthquakes [33]. Motion of the water column at 0.3–0.5 Hz could produce the dip with added energy within the limit the record sets at 0.4–0.5 Hz, and just beyond it at 0.3 Hz (Results). The best fit of added energy explains 41–49% of the dip but cannot be told apart from no added energy (Supplementary Note S2.4), so the record neither requires nor excludes a contribution from the earthquake. A response of the onboard processing to up-and-down motion is conceivable but speculative. Whether Sofar, the manufacturer, filters out motion more rapid than half the buoy's sampling rate, or applies onboard quality control, is undocumented [14,15]. Without such a filter, some of that motion would appear at a false, lower frequency still inside the band and above the waves' average frequency, lowering T_m (Supplementary Methods S1.1).

The 30-min data that drifting wave buoys send by default can at best flag unexpectedly large changes for follow-up; they cannot reveal, let alone trace to an earthquake, the signals expected even above a great rupture. Yet GNSS receivers on ships can detect tsunamis [34,35], and warning systems have adopted new technology after major earthquakes [36].

We recommend that raw sea-surface motion and positions logged on board be retrievable remotely around large earthquakes. Buoys should send wave spectra with every 30-min record and, after a trigger, data at a high rate for minutes to hours, like the event mode of DART stations [7]. Their onboard processing should be documented (Methods). Surface buoys will not replace seafloor pressure gauges [6] or estimates of the tsunami source from DART records [37], but one that happens to drift near an earthquake can add measurements of currents, sea-surface motion and timing in otherwise unobserved places.

The analysis rests on one buoy and one 5-month data series. Using comparison times assumes that, without an earthquake, the earthquake's time would behave like any other, although the buoy crossed different bodies of water. Restricting comparisons to nearby dates, similar conditions or the same time of day reduces but does not remove this concern. Several choices, including the threshold for surviving correction, were made after inspection. The corrections cover only recorded choices, and the out-of-sample test addresses them only partly (Methods). How unusual the drift-speed rise appears varies between background models, and the predictions rest on one fault-slip model without offshore data (Results). No independent observations of currents were examined, and no other instrument measured the waves there during the four arrival records. Five other $M \geq 6$ earthquakes occurred during these records (Table 1), so an effect could not be assigned to one earthquake.

Neither unexplained feature is a detection, but both can be tested. The drift-speed step could be tested with positions and raw sea-surface motion logged on board, with fix times, quality flags and documentation of how and when the transmitted position is formed; spectra alone cannot. The wave-period dip could be tested with 30-min spectra or raw motion of the four arrival records and their neighbours. These data were unavailable, apparently never transmitted and readable only from the buoy's memory card, in practice after recovery [15]. Tests needing no new data from this buoy include the same T_m statistic at other buoys near large earthquakes (Methods), vertical ground motion recorded at similar distances, currents along the track from satellite sea-surface heights, and the tsunami at the buoy computed from an earthquake model fitted to tsunami or DART records.

Methods

Buoy and data product

Spotter, made by Sofar Ocean, is a GPS-based wave buoy, used here drifting freely (unanchored). The summary values that it computes on board (bulk wave parameters) were

within 10% of those of a reference buoy [38]. It derives the displacement of the sea surface from Global Navigation Satellite System (GNSS) signals, which include those of GPS. We assume that the same receiver provides the positions that it reports. By default it samples the displacement 2.5 times per second (2.5 hertz, Hz) for 30 min. From each 30-min series it computes a wave spectrum, which shows how the variance of the vertical displacement (its energy) is spread over frequency. The spectrum gives the variance per unit frequency (a variance density spectrum) in bins of $\Delta f = 2.5/256 \approx 0.0098$ Hz from 0.029 Hz (periods up to about 34 s) [14].

The significant wave height and the mean period are computed from moments of the spectrum, summed over a range of frequencies, the frequency band. The n-th moment is $m_n = \Sigma f^n E(f)\Delta f$, summed over the bins of the band, where f is the frequency of a bin and $E(f)$ its variance density. The zeroth moment, m_0, is thus the variance of the vertical displacement within the band. The significant wave height is $H_s = 4\sqrt{m_0}$, four times the standard deviation of the sea-surface height within the band. The mean period is $T_m = m_0/m_1$ (also written T_{m01}), the inverse of the average frequency of the motion, each frequency weighted by its energy. The peak period T_p, the period of the waves carrying the most energy, is the inverse of the frequency of the most energetic bin. Sofar's documents disagree on the upper limit of the band: the moments end at about 1.24 Hz in the technical reference manual [14] and at 0.8 Hz in the user guide [15]. Spectra from this buoy's pre-deployment test reproduce the H_s and T_m that it reported when the moments are taken over 0.03–0.8 Hz (Supplementary Methods S1.1; Supplementary Fig. S1). We therefore take that band (periods of about 1.25–34 s), although the limit used on board in 2025 is not documented. Motion of the water column at frequencies inside the band would enter the summary values. One example is water-column resonance: sound waves trapped between the seafloor and the sea surface, which ring at frequencies set by the water depth (Supplementary Methods S1.2). Such oscillations were measured in the source area of the 2003 Tokachi-oki tsunami [39,40].

Sofar does not document how the displacement is derived from the receiver's GPS solution, the position and velocity that the receiver computes from the satellite signals. Nor does it document whether the 2.5-Hz series is anti-alias filtered, or any quality control on board (checks that flag or remove bad data). Anti-alias filtering removes motion more rapid than half the sampling rate; without it, such motion appears at a false, lower frequency. Sofar gives the accuracy of the displacement as about ±2 cm [15]. Each 30-min set of summary values is a record, and the satellite position sent with it is its fix. Each record's time stamp marks the

end of its 30-min measurement period, whereas its fix is the location "when the report was encoded and transmitted" [41]. The delay between the time stamp and the fix (the fix delay) is not documented, and neither is whether the position is filtered.

On 13 June 2024, Spotter SPOT-31540C, the buoy used here, sent its first record since its pre-deployment test, from Mekoryuk, Nunivak Island, Alaska. It then drifted south along Kamchatka (buoy data; Data availability). We analysed the file of its data for 1 July–2 December 2025 exported from Sofar's public dashboard, the website on which Sofar displays each buoy's data. This file, the data series of the main text, holds 7,352 records, one every 30 min, with gaps of up to 17.5 h (Supplementary Methods S1.16). Besides H_s, T_m and T_p, each record holds the wave directions and their spreads (how widely the wave energy is spread in direction), the wind (below), the position and engineering channels. The engineering channels are readings of the buoy's own condition: battery voltage, power and the humidity inside its sealed housing (enclosure humidity). Sea-surface temperature (SST) and air pressure are reported hourly, in steps (resolutions) of 0.02 K and 0.1 hectopascal (hPa). The depth of the SST sensor and the interval over which each air-pressure value is averaged are not documented. The wind is not measured but inferred from the wave spectrum (the wave-derived wind), with a root-mean-square (rms) error of about 2 m s^{-1} at wind speeds of 3–12 m s^{-1} [42].

The out-of-sample test (see 'Analyses') was a test on wave data, and on earthquakes, that had not been examined when the test was written down. It also used the buoy's full history of records processed on board (its "embedded" history), from 13 June 2024 to 11 October 2026. This history has a 146-day gap from 30 November 2024 to 26 April 2025, and it matches the analysed file on all the records that both contain (Supplementary Methods S1.16). On 11 October 2026 the dashboard showed firmware (the buoy's onboard software) v2.6.1, the bulk "waves" mode, which sends summary values, and data transmission through the Iridium satellite network (Iridium satellite telemetry). None of the 28,709 records of the deployment carries spectra, although the export holds spectra for the 38 high-data-rate (HDR) records of the pre-deployment test. The 30-min spacing of the records matches the default "Waves: Standard" mode, whereas the "Waves: Spectrum" mode yields one 60-min sample every 1–6 h and the HDR mode requires a mobile-phone (cellular) connection [15,41]. We therefore infer that no spectra were transmitted during the deployment.

The Discussion recommends that buoys send data at a high rate after a trigger. The trigger could come from the buoy itself (internal) or from outside it (external). We also recommend

that each processing step that this subsection reports as undocumented be documented for every firmware version. Air-pressure readings from buoy barometers should be checked against a reanalysis, a reconstruction of past weather (see 'Analyses'), before they are used to look for small signals. GPS positions at 1 Hz or more (at least one position per second) would resolve tsunami currents such as the 0.12–0.18 m s^{-1} predicted here (Results, 'What the fault-slip model predicts and what the buoy could measure'), provided slow movements are not filtered out of them (high-pass filtering).

Earthquakes, geometry and arrival records

Earthquake parameters (the time at which each earthquake began, its location, depth and magnitude) are from the Advanced National Seismic System (ANSS) Comprehensive Catalog (ComCat) of the U.S. Geological Survey (USGS) [43]. Supplementary Table S5 lists all 40 earthquakes used (Supplementary Methods S1.9). The point where a rupture begins is its hypocentre, and the point on the Earth's surface directly above it is its epicentre. The M_w 8.8 earthquake (ComCat identifier us6000qw60) began at 23:24:52.5 Coordinated Universal Time (UTC) on 29 July (the origin time, t_0), with its epicentre at 52.495°N, 160.240°E and its hypocentre 35 km deep [1]. The USGS fault-slip model (a finite-fault model) estimates how far, in which direction and when each patch of the fault moved. Its hypocentre lies 3.9 km from this epicentre and 18 km shallower [44]. The tsunami of the M_w 8.8 reached heights on land (run-ups) of typically 5–10 m above sea level along the Kamchatka and northern Kuril coasts, and locally 10–16 m [5]. The other three earthquakes of magnitude 7.4 or larger ($M \geq 7.4$) are the M_w 7.4 of 20 July, the M_w 7.4 of 13 September and the M_w 7.8 of 18 September 2025. The magnitudes of the five earthquakes listed in Table 1 are all M_{ww}, the W-phase moment magnitude, which the USGS computes from long-period seismic waves (the W phase). The largest aftershock (a smaller earthquake that follows a large one in the same area) in the first day was an M_w 6.9 at 00:09:59.0 UTC on 30 July. Its epicentre was 10.6 km (epicentral distance), and its hypocentre 38.1 km (hypocentral distance), from the buoy position interpolated between fixes to its origin time.

The buoy's 23:25 fix was 52.2 km from the epicentre on a bearing of 215° (measured clockwise from north). This is along the 217° strike of the USGS fault-slip model [44], the compass direction of the line along which the fault meets a horizontal plane. It is also the direction in which the rupture spread, which was largely one way (unilateral rupture propagation) [45]. The water at the fix was 2,671 m deep according to the Global Multi-Resolution Topography (GMRT) synthesis [46], a compilation of seafloor depths. Within 12 h

of the origin time the buoy drifted over the continental slope, in water about 1,880–3,420 m deep. The continental slope is the seafloor that descends from the edge of the continental shelf to the deep ocean floor.

Each record's time stamp marks the end of its measurement period (see 'Buoy and data product'). We therefore define an earthquake's arrival record as the first record stamped at least 60 s after its origin time. It is the 30-min record during which the earthquake's seismic waves (the ground vibrations from the earthquake) reached the buoy. For each earthquake, the arrival times of P, S and Rayleigh waves estimated by treating the earthquake as a single point (a point source) fall inside this record (Table 1). P (compressional) and S (shear) waves travel through the Earth, and Rayleigh waves travel along its surface. For the M_w 8.8 the arrival record is the record stamped 23:55 UTC (measured 23:25–23:55). These arrival times are only approximate for the M_w 8.8, because its rupture lasted minutes. The seismic moment measures an earthquake's size: the rigidity of the rock times the area of the fault times the average slip (how far the two sides of the fault moved past each other). In the USGS fault-slip model, 5, 50 and 95% of the moment had been released 38, 120 and 191 s after the origin time, all within that record. The first P waves reached the sea surface at the buoy 8–12 s after the origin time (Table 1, note a). The 23:25 fix, taken at or after 23:25:00, may therefore already have been affected by the shaking.

Had the time stamps marked the start of the measurement period instead, the seismic waves would have reached the buoy during the record stamped 30 min earlier. We call these two records the candidate records of an earthquake (stamped 23:25 and 23:55 UTC for the M_w 8.8). Both were examined before we had checked the time-stamp convention. The choice between them is therefore part of the recorded search, the statistics and analysis choices that we evaluated and recorded (see 'Statistical framework'; Supplementary Methods S1.10; Supplementary Table S6).

None of the tsunamis of the other three $M \geq 7.4$ earthquakes could have reached the buoy before their arrival records ended. These records ended 6, 17 and 27 min after the origin times of the earthquakes of 20 July, 13 September and 18 September (Table 1). A tsunami travels as a long wave (a wave much longer than the water depth), at the long-wave speed $\sqrt{(gh)}$, where g is the acceleration due to gravity and h the water depth, so it travels faster in deeper water. The deepest water on the profile of Fig. 1c, the depth profile through the buoy, is 7,909 m deep, where $\sqrt{(gh)} \approx 0.28$ km s^{-1}. Even travelling at that speed along its whole path, a tsunami

starting at each epicentre would have needed about 13, 37 and 44 min to cover the 216.5, 621.1 and 739.4 km to the buoy.

Forward model of deformation and near-field tsunami

From the USGS fault-slip model [44] (model 1, version 5; M_w 8.83) we computed the displacement of the seafloor during the earthquake (coseismic deformation) and the tsunami close to the source (the near field). These are forward models: they compute what the fault-slip model predicts, without adjusting it to any observation. The fault-slip model consists of three fault segments, all striking 217° and dipping (inclined below the horizontal) at 6.5°, 17° and 28°, which are divided into subfaults (fault patches) of 20 × 10 km. For each subfault it gives the slip, the rake (the direction of the slip within the fault plane) and the rupture time (when the subfault began to move). We computed the seafloor displacement with Okada's [47] solution for a rectangular dislocation (slip on a rectangular patch of fault) in an elastic half-space, a uniform elastic solid below a flat surface. The computation used the slip, rake and rupture time of each subfault. Within 50 km of the buoy the result reproduces the USGS surface-deformation grid for this model to 1.9 cm rms.

The uplift of the seafloor was converted to the initial displacement of the sea surface, η_0, with the $1/\cosh(kh)$ low-pass filter [40,48] (ref. 21, ch. 3). Here k is the horizontal wavenumber (2π divided by the horizontal wavelength) and h the water depth. The filter represents the smoothing by the water above: it passes broad features of the uplift and damps features only a few water depths wide or narrower. Where the seafloor slopes, its horizontal movement also raises or lowers the water above it [49]. We evaluated this contribution along the GMRT depth profile through the buoy (Fig. 1c) and on the GMRT depth grid. At the buoy the model gives a seafloor displacement of +0.10 m vertically and 3.88 m horizontally toward 127°. Along a line through the buoy in that direction, the seafloor rises (uplift) by up to +3.7 m about 20 km seaward of the buoy. It sinks (subsidence) by up to −1.5 m 19 km landward. The hinge line separates the area of uplift from the area of subsidence. In variants of the USGS model with other fault geometries, or with the subfault depths reduced by the water depth at the buoy, so that the fault lies closer to the flat surface of the elastic half-space (depth-reference variants), the hinge line lies 0.2–4.5 km from the buoy. After filtering, the line where η_0 is zero lies 1.0 km from the buoy, and the filtered η_0 at the buoy is small, 0.14–0.15 m. Including the contribution of horizontal displacement, η_0 at the buoy is 0.1 ± 0.1 m.

We computed the tsunami's sea-surface elevation η, its current and the water-parcel displacement at the buoy with five implementations of linear tsunami models (Supplementary Methods S1.15; Supplementary Table S8). The water-parcel displacement is how far the tsunami's currents carry a parcel of water, and a buoy floating in it; between two fixes, it is the tsunami water movement of the main text. Linear models treat the tsunami's height as small compared with the water depth. The reference implementation, I1, is the exact solution of the linear equations at constant depth, computed in Fourier space, that is, as a sum of waves of every wavenumber. It is run either dispersive, with waves of different lengths travelling at different speeds, or in the long-wave approximation, in which all travel at $\sqrt{(gh)}$. Its source is either kinematic, releasing the uplift of each subfault at its time in the rupture, or instantaneous, releasing all of the uplift at once. One-dimensional variants compute the tsunami along the GMRT profile only. I2–I4 are separately written finite-difference codes, which solve the shallow-water equations (the equations for waves much longer than the water depth) on a grid of points. They use constant depth or plane-parallel depth (taken from the GMRT profile and held constant along the strike), alternative fault geometries, and the source shifted by ±15 km. I5 is a finite-difference run on the two-dimensional GMRT depth grid close to the source, with plane-parallel depth elsewhere.

The drift-speed step is the change in drift speed from the drift interval (the 30 min between two consecutive fixes) ending at the 23:25 fix to the interval ending at the 23:55 fix. We compared it with the tsunami's contribution to it, $\xi(t_2) - 2\xi(t_1)$. Here ξ is the water-parcel displacement since the origin time along the drift direction after the step (208°), and t_1 and t_2 are the times of the two fixes that bracket the arrival record. With no fix delay they are 7.5 s and 1,807.5 s after the origin time; fix delays of 0–300 s were allowed. The tsunami moves no water before the origin time, and the first interval began before it. The tsunami therefore adds $\xi(t_1)$ to the buoy's movement along the drift in the first interval, and $\xi(t_2) - \xi(t_1)$ in the second. The difference, $\xi(t_2) - 2\xi(t_1)$, is its contribution to the step, expressed as a distance moved along the drift in 30 min. With no fix delay, the modelled net displacement between the two fixes points 114–145° from the drift direction after the step (Supplementary Fig. S4). With fix delays of up to 2 min, it points up to 166° from that direction. With a fix delay of 300 s, the net displacement between the fixes in the finite-difference runs points toward 355–062°, on either side of the direction opposite to the drift (028°). In the two-dimensional runs, the largest excursion within 2 h, the largest distance that a water parcel moves from its starting point, is 50 m. It falls short by a factor of 4.8 of the +241 m of extra movement of the buoy

along the drift that the step requires. Over all runs that computed it, including the one-dimensional ones, the excursion within 2 h is at most 60 m (Results, 'What the fault-slip model predicts and what the buoy could measure'; Supplementary Table S8), so even ignoring direction the tsunami's largest movement of water is at least 4.0 times too small. What limits the movement is the short duration of the currents, not the height of the sea level. Near the hinge line the models give 2.6 times more current per metre of sea-surface elevation than a progressive long wave. A progressive long wave is a single long wave travelling in one direction; its current is its height times $\sqrt{(g/h)}$. A limitation of these predictions is that all five implementations are linear and only one (I5) uses two-dimensional bathymetry (seafloor depth mapped in both horizontal directions).

Deep-ocean Assessment and Reporting of Tsunamis (DART) stations record tsunamis with a pressure gauge on the seafloor. We tested the fault-slip model, as a tsunami source, against DART 21416, 534 km from the epicentre in 5,789 m of water. This station is run by the National Data Buoy Center of the U.S. National Oceanic and Atmospheric Administration (NOAA NDBC) [7]. We used its 1-min water-column heights from the historical DART files [50]: the height of the water above the gauge, derived from the seafloor pressure. We de-tided them (removed the tide) with a harmonic tide model. This model represents the tide as a sum of tidal constituents, oscillations whose periods are fixed by the motions of the Moon and the Sun. We fitted it by least squares (minimising the sum of the squared misfits) to the station's 15-min data from 11 July to 28 August 2025. This period runs from the start of the station's current deployment to 30 days after the origin time. The fit used 10 tidal constituents and left out the period from 1 h before to 48 h after each $M \geq 7.4$ earthquake (Supplementary Methods S1.15).

The tsunami arrived at the station 27.7 min after the origin time, and its first crest, +0.85 m, came at 32 min (Supplementary Fig. S12; Supplementary Table S9). The finite-difference models I3–I5 predict the onset (the arrival) to within 2.3 min. But they over-predict the first crest of the 1-min values by a factor of 2.0–2.7 (1.68–2.29 m), and the following trough by a factor of 3.1–3.6. These models are non-dispersive: they let all wave components travel at the long-wave speed. Allowing for their non-dispersive propagation, the fault-slip model over-predicts the first crest by a factor of about 1.5–2.2. Its peak uplift (8.2 m) is also about twice that of a source fitted to DART records (DART-constrained) and built from smoother unit sources (about 4 m) [2]. Unit sources are standard fault patches whose precomputed tsunamis are scaled and summed to fit the records. The comparison therefore tests the fault-slip model

738 together with an idealised, non-dispersive path to the station. The predictions at the buoy,
739 close to the source, probably overestimate the motion, although this scaling, measured far
740 from the source, has not been shown to hold at 52 km from the epicentre.

741 **Statistical framework**

742 All significance statements in this paper rest on empirical nulls. Each statistic computed at an
743 earthquake was computed in exactly the same way at every other admissible time of the 1
744 July–2 December 2025 data series. An admissible time is one at which the data that the
745 statistic needs exist and that lies outside the exclusion windows described below. The
746 admissible times are the null times (the comparison times of the main text), and the values of
747 the statistic at them form its empirical null distribution, or null. The one-sided p-value is $p = (k + 1)/(N + 1)$. Here N is the number of null values, and k is the number of them at least as
748
749 extreme as the value at the earthquake, in the claimed direction of the anomaly (the departure
750 from ordinary behaviour being tested). Ties count as at least as extreme. Adding one to both
751 counts treats the earthquake as one more member of the null, so p is never zero. The test
752 assumes that, without an earthquake, the earthquake's time would behave like any null time
753 (the times are exchangeable; Discussion).

754 Times near earthquakes were excluded from the nulls (Supplementary Table S10). These
755 exclusion windows are mostly ±12 h or ±24 h around the origin times of the four $M \geq 7.4$
756 earthquakes. For statistics of a single wave record, they are ±12 h around each of the 31 $M \geq 6$
757 earthquakes of the data series in 40–60°N, 150–170°E. The null times cover the continental
758 margin off Kamchatka, where the buoy drifted until 22 September, and the open North Pacific
759 thereafter. Null values at neighbouring times resemble each other (they are serially
760 correlated), and the buoy crossed different water masses, bodies of water with different
761 properties. We therefore also used local nulls, restricted to times within ±7 or ±15 days of the
762 earthquake. We also used conditioned nulls, restricted to times with a state similar to that
763 before the earthquake, for example in wave height and period, or to times at about the same
764 time of day. Quoted ranges of p span these choices. A moving-block bootstrap [51] estimates
765 the sampling uncertainty of p. It resamples the null values many times in blocks of 48
766 consecutive values, i.e. 24 h, which keeps the correlation within each block, and recomputes p
767 for each resample.

768 The anomalies examined here were found by inspecting the data series, so the nominal p of a
769 single statistic (the uncorrected p of the main text) overstates the evidence. We therefore

grouped the statistics evaluated at the M_w 8.8 into families, groups of related statistics that are corrected together (Supplementary Methods S1.12; Supplementary Table S7). The family-wise p of a family is the single-step min-p adjustment [52], (m + 1)/(N + 1). Here m is the number of null times at which the smallest p over the family is at least as small as the smallest p at the earthquake. At each null time, the p of every statistic is computed against all other times, the earthquake included, exactly as at the earthquake (exceptions: Supplementary Methods S1.12). Every statistic of the family is evaluated at the same null times, so this adjustment preserves the dependence between statistics: correlated statistics are not penalised as if they were independent. For a named member, one particular statistic of the family, m counts the null times at which the family's smallest p is at least as small as that member's p at the earthquake. Family-wise control limits the probability that any statistic of a family appears unusual by chance. We ask whether any of a few features is real, so we prefer this conservative control to control of the false-discovery rate [53], the expected proportion of chance results among the statistics flagged. Wilks [54] recommends the false-discovery rate for field significance, the joint assessment of tests at many points of a map. The p-values of several earthquakes were combined into one, the Fisher p of the main text, with Fisher's method. This method uses minus twice the sum of the natural logarithms of the p-values; it is one of several possible ways of combining them [55]. An omnibus test (the combined test of the main text) asks whether the buoy's data, taken together, are unusual at the origin time. It combines the p-values of the candidate features (see 'Analyses') with Fisher's method. The result is judged against the same combination computed at every null time, rather than against a theoretical distribution.

We call a family-wise p small if it is below 0.05. We set this threshold, and the conditions for a detection given below, during revision of the manuscript, after the results were known. The verdicts on the two unexplained features are the same for any threshold between 0.02 and 0.1. In one sensitivity test, a repeat of the correction with a different null for some drift statistics, they are the same between 0.032 and 0.1 (Supplementary Note S2.6). The rule applies only to features named before the correction was run. It also applies only to family-wise p judged against nulls that respect any day–night cycle (for a quantity with such a cycle, null times at about the same time of day, or values with the cycle removed). Two values below 0.05 fall outside it. One is the family-wise p of the range of the hourly air-pressure readings spanning the earthquake (the flat stretch of the main text) against all times (0.025). That null ignores the day–night cycle (see Results, 'Sea-surface temperature, air pressure, wave-height scatter and

combined tests'). The other is more wave-height scatter (H_s scatter, the variation of H_s from record to record) after the other three M ≥ 7.4 earthquakes. Its family-wise p is about 0.03 over the 351 statistics of the three-earthquake search behind the wave-period dip (see 'Analyses'). This set differs from the 351 statistics recorded at the M_w 8.8; the two counts coincide by accident (Supplementary Methods S1.12). The pattern lies in the direction that the original analysis had not tested: that analysis looked for less scatter after the earthquake. The pattern was found while the correction was being run, and it is absent at the M_w 8.8 (Supplementary Note S2.4). The recorded search comprises every statistic and analysis choice that we evaluated and recorded. A feature with a small family-wise p over the full recorded search is reported as surviving correction for the recorded search, not as a detection. A detection would also require (i) a statistic fixed before the data used to test it were examined, or replication ($p \leq 0.05$) in independent data with the statistic fixed in advance; and (ii) a physical mechanism that predicts its sign and approximate size. A family-wise correction can include only the analysis choices that left a record (Supplementary Tables S6 and S7). Choices tried but not recorded cannot be counted, so every family-wise p in this paper is a lower bound.

For the detection limits (Results, 'Detection limits: how large a change the data could reveal'), c is the critical value, which a statistic must exceed to reach one-sided $p \leq 0.05$ against its null. Suppose an anomaly of fixed size is added to the statistic at a randomly chosen null time. The sum exceeds c with probability 0.5 if the anomaly equals δ_{50} = c minus the null median. It exceeds c with probability 0.8 if the anomaly equals δ_{80} = c minus the null's 20th percentile (Supplementary Methods S1.3; Supplementary Table S1). The main text calls δ_{50} the detection limit. For the 30-min drift-speed step, δ_{50} equals c, because the median step at the null times is close to zero (Supplementary Table S1). For air pressure, the averaging interval of the hourly readings is not documented. If each reading is a 1-h mean, a limit in pascals becomes a limit on the product of a pulse's height and its duration (an amplitude–duration product), in pascal seconds (Pa s; Supplementary Methods S1.3). A pressure pulse would then reach $p \leq 0.05$ with probability 0.5 only above 1.0–1.5 × 10^5 Pa s, or above 1.5–2.0 × 10^5 Pa s relative to ERA5, the reconstruction of past weather described in 'Analyses'. Physically based scenarios for the air-pressure waves set off by the earthquake give 0.8–7 × 10^3 Pa s (Supplementary Fig. S2; Supplementary Note S2.3), 14–260 times below these 50% limits (Supplementary Table S1). These limits hold for one statistic tested alone; a change sought among several statistics would have to be larger.

Analyses

Drift. Drift velocities were computed from consecutive fixes and are labelled by the end of each interval between them. Spotters drift like drogued drifters (drifters with an underwater drag element, a drogue, that makes them follow the near-surface current), with about 1% windage [13]. Windage is the part of a drifting buoy's motion caused directly by the wind, as a fraction of the wind speed. We therefore interpret the drift as near-surface current plus a small wind and wave contribution. Around the earthquake, the wind estimated from the waves (the wave-derived wind) exerted a stress, the wind's push on the sea surface per unit area, of ≤ 0.033 N m^{-2}. This value assumes a drag coefficient extrapolated below the range of wind speeds in which it was measured [56] (Supplementary Note S2.1). The drag coefficient is the factor that relates the stress to the density of air times the square of the wind speed.

Background models are statistical models of the buoy's ordinary drift. They describe the complex velocity u + iv, where u is the eastward and v the northward component; this form makes rotating currents simple to represent. The models were fitted over 20 July–8 August to predict the 12 h after t_0 (Supplementary Methods S1.4; Supplementary Table S3). The fit excluded t_0 − 1 h to t_0 + 12 h and the same window around the origin times of the other three M ≥ 7.4 earthquakes; these excluded hours are the event windows. The trend model, specified first, has a background flow with a linear trend, a clockwise near-inertial oscillation, four tides and the wave-derived wind. A near-inertial oscillation is a rotation of the upper-ocean current, clockwise in the Northern Hemisphere, at a period close to the local inertial period, which is set by the Earth's rotation and the latitude. Such oscillations are found almost everywhere in the upper ocean [57], and the buoy's drift shows them (Supplementary Note S2.1). The cross-validated background model (the preferred background model of the main text) has a background flow that varies smoothly in time (a spline, a curve made of polynomial pieces joined smoothly), the near-inertial oscillation and lagged wind (the wind at the same time and at earlier times). It was chosen among 102 configurations, combinations of such terms, by cross-validation: by how well each predicted drift left out of its fit at many other times. The event windows never entered this choice, but the choice was made, and the set of configurations defined, after the data series had been inspected. The statistic tested is the 12-h excess, the mean of observed minus modelled speed over the predicted period. Its null repeats the same exclude–fit–predict procedure at every other 30-min null time (N = 6,376): leave out the hours around that time, fit the model to the rest of a span of the same length and position relative to that time as the span fitted for t_0, and predict the hours left out.

A causal forecast, which uses only data from before the time it predicts, was tested in the same way; it was fitted to $t_0 - 3$ d to $t_0 - 1$ h only.

The drift-speed step compares the first drift interval after the origin time (23:25–23:55), which coincides with the arrival record, with the preceding interval (22:55–23:25). At the assumed fix times (no delay), that interval ends 7.5 s after the origin time and so contains it. We also asked whether a single displaced fix could produce the step. The departure of the 23:25 fix from a smooth track through the neighbouring fixes was ranked among the departures of all other fixes (Supplementary Methods S1.4). These departures combine fix error with real motion of the buoy over less than an hour. Fix errors as large as the departure of the 23:25 fix are therefore probably no more common under ordinary conditions than the ranking implies. The ranking says nothing about fix errors during strong shaking, whose size is unknown. Because the timing of fixes is not documented, a late 23:55 fix could also mimic the step. At constant speed, however, it would need a delay of about 12 min, followed by a drop in speed to about 0.2 m s^{-1} in the next interval. Speed instead kept rising, which argues against a delayed 23:55 fix. Over the whole data series, 30-min velocity changes mostly reflect ocean motion rather than position noise. Their lag-1 autocorrelation, the correlation between each change and the next, is +0.46, whereas uncorrelated position noise would give −0.67. The change of the velocity vector across the step has a component of 0.04–0.05 m s^{-1} perpendicular to the trench (trench-normal).

At the other three $M \geq 7.4$ earthquakes, the step into the interval that coincides with the arrival record, as at the M_w 8.8, gives $p = 0.46$–0.55 (Table 2). The step into the interval that begins at the first fix after the origin time gives $p = 0.45$–0.99. The step into the interval containing the M_w 6.9 aftershock (+0.068 m s^{-1}, $p \approx 0.08$) starts from the elevated speed of the 23:55 interval, so it is not an independent control. The modelled tsunami contributes at most +0.019 m s^{-1} to it.

A broad search, the 24-feature search of the main text, tested candidate features of drift, waves, wind, engineering channels, SST and air pressure at the M_w 8.8. Its null holds 6,748 times (Supplementary Methods S1.12; Supplementary Table S7). One drift feature was added after the data around the origin time had been inspected, and the step-plus-rise combination later (see Results, 'The drift-speed step just after the earthquake'). This combination was tested because the step began the rise in drift speed noticed by eye. It is a step at least as large as observed followed by a 6-h rise in mean drift speed at least as large as observed (0.29 m s^{-1}; Supplementary Table S12). Once a step has occurred, such a rise is unremarkable. Of the

902 50 null steps at least as large as the observed step, 12 were followed by such a rise (11 of 47
903 in the null of Fig. 4a).

904 **Wave statistics.** For T_m and H_s, a record's residual is its value minus the mean of its two
905 neighbouring records, the records just before and after it. Dividing the residual by a robust
906 local scale gives z, the residual z of the main text. The scale is 1.4826 times the median
907 absolute deviation of such residuals within ±24 h (N = 6,442 null records for T_m;
908 Supplementary Methods S1.7). The median absolute deviation is the median distance of
909 values from their median. The factor makes the scale equal to the standard deviation for
910 normally distributed values, while outliers barely affect it. The main text also gives a
911 corrected p for the M_w 8.8 (Results, 'Mean wave period and wave height: the wave-period
912 dip'). It allows for either candidate record, the arrival record or the record before it
913 ('Earthquakes, geometry and arrival records'), and for a departure of either sign. Its statistic is
914 the larger |z| of the two candidate records, and its null is the same statistic for pairs of
915 consecutive records. If the sea-surface elevation is a Gaussian (normally distributed) random
916 process, the spectral estimates computed from a record scatter about their true values with an
917 approximately chi-square distribution [58,59]. H_s and T_m in one record come from the same
918 estimates, so their sampling errors are correlated. We quantified this correlation by the
919 regression of z_{Hs} on z_{Tm} over the null records. We also bounded the in-band variance that
920 shaking could have added, using the H_s and T_m of the M_w 8.8 arrival record together
921 (Supplementary Methods S1.7). In-band variance is extra variance of the sea surface within
922 the frequency band of the summary values (the added energy of the main text). In that record
923 H_s was close to the value that its low T_m predicts through the correlation between their
924 sampling errors, so the two together exclude all but a small added variance (Results,
925 'Detection limits: how large a change the data could reveal'; Supplementary Note S2.4).

926 **The wave-period dip across earthquakes.** The statistic of the wave-period dip is the one-
927 sided T_m z of the arrival record. In the Supplementary Information this feature is called the
928 arrival-record T_m dip. The pattern was noticed at the M_w 8.8, so it is judged on the other three
929 M ≥ 7.4 earthquakes, whose p-values are combined with Fisher's method. This statistic was
930 adopted after 105 statistics of the wave records had been evaluated at all four earthquakes,
931 together with 246 statistics of the separate air-pressure, H_s-scatter, SST and drift analyses.
932 Together these form the three-earthquake search. To obtain its family-wise p, we drew
933 random sets of three admissible times and treated each set exactly like the three earthquakes,
934 with every statistic recomputed against its own null. The family-wise p is the fraction of

random sets whose smallest Fisher p over these statistics is at least as small as at the earthquakes. A specification curve, the three-earthquake Fisher p for each defensible definition of the residual (the departure of a record from the records around it), shows how the result depends on that choice (Supplementary Methods S1.10; Supplementary Table S6).

Three further tests are ones in which a real effect would also predict dips. The first uses the 18 other $M \geq 6$ earthquakes of 2025 in the region defined in 'Statistical framework' that lie in records of their own. Of these records, 17 have a z, because one fell in a data gap (Supplementary Methods S1.9; Supplementary Table S5). The second is the arrival record of the M_w 6.9 aftershock. The third is an out-of-sample test. Earthquakes are ordered by $L = M - 1.66 \log_{10} \Delta$, where M is the magnitude and Δ the epicentral distance in degrees (the angle at the Earth's centre). L is a crude proxy for the amplitude at the buoy of seismic surface waves (seismic waves that travel along the Earth's surface); it serves mainly to order earthquakes. The out-of-sample test used records from outside the data series and a protocol fixed in advance: a written plan that set the statistic, the rules for choosing earthquakes and data, and the decision rule (Supplementary Methods S1.11). The protocol was written to a local file on 11 October 2026, before any wave values or catalogue earthquakes outside July–December 2025 had been examined. It was not registered externally (with a third party), and the test was run minutes later (see Results, 'Mean wave period and wave height: the wave-period dip'). The protocol admitted every $M \geq 6.5$ earthquake whose epicentre lay within 1,500 km of the buoy, if its arrival record and both neighbouring records existed and passed checks of validity made without looking at z (Supplementary Methods S1.11). Its decision rule fixed the verdict in advance: replication if the Fisher p is at most 0.05; failure if it is above 0.05 and the power (defined below) for a shift of the observed size is at least 0.80; inconclusive otherwise. The protocol also converts differences in L into amplitude ratios, a speculative scaling that gives the factors by which the two out-of-sample earthquakes were weaker and one power scenario (Supplementary Methods S1.11). One further earthquake of magnitude about 7.4 or more within about 750 km of any drifting Spotter would test the pattern with the T_m of the transmitted summary values alone. Power is the probability that a test gives one-sided $p \leq 0.05$ if an effect of a stated size is really present. For that one-earthquake test it would be about 0.8 if the true shift of z equals the mean shift at the three earthquakes (the in-sample mean), which selection probably inflates. It would be about 0.36 at the less negative end of the 95% interval of that mean.

Other variables and reanalysis. SST was tested as its rise from 09:58 to 17:58 local apparent solar time (LST, time by the Sun at the buoy; the origin time was 09:58 LST on 30 July). The rise was compared with the same rise on all other July–September days and on the 16 other calm days, days with weak wave-derived wind. On 30 July SST rose under a mean wave-derived wind of 2.4 m s^{-1}. Air pressure was analysed as residuals from local trends and from an empirical day–night cycle fitted to the data, made of a daily (diurnal, S_1) and a twice-daily (semidiurnal, S_2) harmonic, each a sine-shaped cycle with a fitted amplitude and phase. This cycle is probably an instrument effect. It is absent from ERA5 (see below), and it is roughly opposite in phase to the small daily swing of air pressure caused by the Sun's heating of the atmosphere, in its long-term average over the ocean (the climatological oceanic pressure tide) [60] (Supplementary Note S2.3; Supplementary Fig. S7). Wave-height scatter was measured as the scatter of H_s from record to record about a running median over a few hours. Swell, long-period waves from a distant storm, was traced by its dispersion [22]. In deep water, longer-period waves travel faster and so arrive first. The peak frequency of a swell, the frequency that carries most of its energy, therefore rises steadily with time, at a rate set by the distance to the storm. Supplementary Methods S1.5–S1.8 give the details of these analyses.

We used hourly data from ERA5, the fifth-generation reanalysis of the European Centre for Medium-Range Weather Forecasts (ECMWF) [61,62]. A reanalysis is a reconstruction of past weather that combines a weather model with observations. The data were taken through the Open-Meteo interface [63] at the point of the 0.25° grid nearest the buoy's daily-mean position. They give context, controls for wind shifts and weather fronts, and a reference for air pressure; no main null test depends on them (Supplementary Methods S1.13). Because estimates of the sunlight reaching the sea surface (insolation) for 30 July differ, the SST rise was also compared with two calculations of daytime warming in a thin surface layer (warm-layer schemes). The first is a rotating bulk-Richardson scaling after Price et al. [21], named after the bulk Richardson number, a ratio of the warm layer's stability to the stirring by its current. It derives the depth of the warm layer from the heat absorbed and from the accumulated wind momentum, which rotates like a near-inertial oscillation. The second is a warm-layer scheme of the type used in the algorithm of the Coupled Ocean–Atmosphere Response Experiment (COARE) for the exchange of heat and momentum between air and sea, after Fairall et al. [23]. Both used the ERA5 wind and were forced with surface shortwave radiation (sunlight) retrieved by the Japan Aerospace Exploration Agency (JAXA)

from images of the Himawari-9 weather satellite [64]. They were also forced with fields of the ECMWF Integrated Forecasting System (IFS), the centre's operational forecasting model (Supplementary Methods S1.14; Supplementary Note S2.2).

Verification, reproducibility and use of AI tools

Each analysis was re-implemented from the raw data files in separately written code, and a third set of scripts produced the figures from the verified values. Where implementations differ, we give the range of results. Supplementary Methods S1.16 and Supplementary Tables S10 and S11 list the parameters, the seeds of the random draws, the software and the file checksums, which let a reader verify that a file is unchanged.

Use of AI tools. An AI assistant (Claude, Anthropic; used in October 2026) was used under the direction and oversight of the corresponding author for three tasks: (i) writing analysis and figure code, which was validated by re-implementing every analysis in separately written code and comparing the results, and whose outputs the corresponding author reviewed; (ii) language polishing and copy editing for a general readership; and (iii) drafting sections from our results and input. All references were checked against their sources. All figures are plots generated by these scripts from the data. The authors designed the study and decided the interpretation and conclusions, and the authors take full responsibility for the content.

Data availability

- **Buoy data.** The embedded-history export of SPOT-31540C is public on the Sofar Spotter dashboard (https://spotter.sofarocean.com/public/SPOT-31540C, "Download data CSV"; no login required). The main analysis uses 1 July–2 December 2025 (7,352 records). The deployment history (Methods, 'Buoy and data product') and the out-of-sample test (Results, 'Mean wave period and wave height: the wave-period dip') use the full history from 13 June 2024 to 11 October 2026 (28,709 deployment records; downloaded 11 October 2026). Supplementary Methods S1.16 gives SHA-256 checksums of both files. The two files are not published with this article or in the code deposit [67], because Sofar Ocean's Terms of Use (https://www.sofarocean.com/legal/terms-of-use) do not explicitly permit public redistribution of dashboard exports. Sofar may reprocess records, and the full history was merged from monthly downloads, so a new download may not be byte-identical.
- **Requests.** Exact copies of both buoy files, as analysed, are available from both authors on reasonable request. A request by email is sufficient; no formal application

or data use agreement is required, and the files are shared subject to Sofar Ocean's Terms of Use. Point of contact: Christopher Maio, University of Alaska Fairbanks, Department of Geosciences, Fairbanks, Alaska, USA; cvmaio@alaska.edu.

- **Earthquake data.** ComCat [43] (https://doi.org/10.5066/F7MS3QZH; accessed 11 and 13 October 2026; event IDs in Table 1 and, for all 40 events used, Supplementary Table S5); finite-fault model us6000qw60_1, model 1, version 5, updated 19 November 2025 [44]; ShakeMap version 18 [32].
- **Bathymetry.** GMRT synthesis [46] from its point, profile and grid services (grid 50.5–54°N, 157.5–162.5°E; https://www.gmrt.org; CC BY 4.0). Version 4.5.0 (June 2026) was current at access, but the services report no version per query.
- **DART data.** Water-column heights for 2025 at DART stations 21416, 21419, 21415 and 21414 [50] (e.g. https://www.ndbc.noaa.gov/data/historical/dart/21416t2025.txt.gz, accessed 11 October 2026); station metadata from NOAA NDBC [65].
- **Reanalysis.** ERA5 hourly single-level data [61,62], retrieved 11–12 October 2026 via the Open-Meteo archive interface [63]. Contains modified Copernicus Climate Change Service information 2026. Neither the European Commission nor ECMWF is responsible for any use that may be made of the Copernicus information or data it contains.
- **Satellite insolation and IFS.** Himawari-9 surface shortwave radiation (Japan Meteorological Agency and JAXA) [64] and ECMWF IFS fields for 26 July–2 August 2025, retrieved 11 October 2026 via the Open-Meteo satellite and historical weather archives [63].
- **Coastlines.** Natural Earth [66], public domain.
- **Derived data.** Supplementary Data S1 (XLSX; one sheet per table) holds the derived data tables: the 40 earthquakes of Supplementary Table S5 with their roles in the analyses, the members of the search ledger (Supplementary Table S7), the test statistics behind Table 2 and Supplementary Table S12, the statistic families of Supplementary Table S6, and the null sizes and exclusion windows of Supplementary Table S10. The buoy files themselves are not included (see 'Buoy data' and 'Requests').

- **Data not used.** For the deployment, the public export holds one position per 30-min record and no spectra, partitions or displacement time series. Spotter logs displacement time series, spectra and positions on an SD card readable only with physical access to the buoy [15]. No SD-card records were used in this study, and the authors hold none, so none can be supplied on request. SPOT-31540C had not been recovered and was still transmitting at 50.29°N, 175.05°E on 11 October 2026; whether its card still holds the 2025 event windows is unknown.

Code availability

All analysis scripts, separately written re-implementations, forward-model code, intermediate results, figure scripts, the protocol of the out-of-sample test (Methods, 'Analyses'), a map from each script to the results it produces and SHA-256 checksums of every file are deposited at Zenodo under the reserved DOI https://doi.org/10.5281/zenodo.23651939 [67]. Until publication, editors and reviewers can access the deposit through a private link supplied with the submission. On publication it will be made public, without access restrictions, under the MIT licence. Supplementary Methods S1.16 lists the parameters, random seeds and software.

References

1. U.S. Geological Survey. M 8.8 – 2025 Kamchatka Peninsula, Russia Earthquake (event us6000qw60). *ANSS Comprehensive Earthquake Catalog (ComCat)* https://earthquake.usgs.gov/earthquakes/eventpage/us6000qw60 (2025).
2. Ruiz-Angulo, A. et al. SWOT satellite altimetry observations and source model for the tsunami from the 2025 M 8.8 Kamchatka earthquake. *Seism. Rec.* **5,** 341–351 (2025).
3. Zhu, Y., An, C. & Yue, H. Trench-breaching rupture of the 2025 M_w 8.8 Kamchatka earthquake and how it repeats the 1952 event. *Geophys. Res. Lett.* **53,** e2025GL120533; https://doi.org/10.1029/2025GL120533 (2026).
4. Sepúlveda, I. et al. SWOT detects dispersive tsunami tied to a near-trench source in the 2025 Kamchatka earthquake. *Science* **391,** 1368–1372 (2026).
5. Pinegina, T. K. et al. Tsunami from the M_w 8.8 Kamchatka earthquake of 29 July 2025 on the east coast of Kamchatka and the North Kuril Islands. *Pure Appl. Geophys.* **183,** 1–25 (2026).
6. Rabinovich, A. B. & Eblé, M. C. Deep-ocean measurements of tsunami waves. *Pure Appl. Geophys.* **172,** 3281–3312 (2015).

7. NOAA National Data Buoy Center. Deep-ocean Assessment and Reporting of Tsunamis (DART) description. https://www.ndbc.noaa.gov/dart/dart.shtml (accessed 11 October 2026).

8. Maeda, T., Furumura, T., Sakai, S. & Shinohara, M. Significant tsunami observed at ocean-bottom pressure gauges during the 2011 off the Pacific coast of Tohoku Earthquake. *Earth Planets Space* **63,** 803–808 (2011).

9. Aoi, S. et al. MOWLAS: NIED observation network for earthquake, tsunami and volcano. *Earth Planets Space* **72,** 126; https://doi.org/10.1186/s40623-020-01250-x (2020).

10. Kato, T., Terada, Y., Nishimura, H., Nagai, T. & Koshimura, S. Tsunami records due to the 2010 Chile earthquake observed by GPS buoys established along the Pacific coast of Japan. *Earth Planets Space* **63,** e5–e8 (2011).

11. Kato, T. et al. Development of GNSS buoy for a synthetic geohazard monitoring system. *J. Disaster Res.* **13,** 460–471 (2018).

12. Kawai, H., Satoh, M., Kawaguchi, K. & Seki, K. Characteristics of the 2011 Tohoku tsunami waveform acquired around Japan by NOWPHAS equipment. *Coast. Eng. J.* **55,** 1350008; https://doi.org/10.1142/S0578563413500083 (2013).

13. Houghton, I. A. et al. Performance statistics of a real-time Pacific Ocean weather sensor network. *J. Atmos. Ocean. Technol.* **38,** 1047–1058 (2021).

14. Sofar Ocean. Spotter technical reference manual. https://content.sofarocean.com/hubfs/Technical_Reference_Manual.pdf (accessed 13 October 2026).

15. Sofar Ocean. Spotter user guide (Document MA-00008-05, Rev. A). https://content.sofarocean.com/hubfs/Spotter%20product%20documentation%20page/2026_Spotter%20Product%20Documentation/Spotter%20User%20Guide.pdf (2026).

16. Geller, R. J. Earthquake prediction: a critical review. *Geophys. J. Int.* **131,** 425–450 (1997).

17. Mulargia, F. & Gasperini, P. Evaluating the statistical validity beyond chance of 'VAN' earthquake precursors. *Geophys. J. Int.* **111,** 32–44 (1992).

18. Gross, E. & Vitells, O. Trial factors for the look elsewhere effect in high energy physics. *Eur. Phys. J. C* **70,** 525–530 (2010).

19. Hu, G., Heidarzadeh, M., Mulia, I. E. & Watada, S. Transoceanic propagation of the tsunami from 2025 M_w 8.8 Kamchatka earthquake across the Pacific Ocean. *Ocean Eng.* **359,** 125915; https://doi.org/10.1016/j.oceaneng.2026.125915 (2026).

20. D'Asaro, E. A. The energy flux from the wind to near-inertial motions in the surface mixed layer. *J. Phys. Oceanogr.* **15,** 1043–1059 (1985).

21. Price, J. F., Weller, R. A. & Pinkel, R. Diurnal cycling: observations and models of the upper ocean response to diurnal heating, cooling, and wind mixing. *J. Geophys. Res.* **91,** 8411–8427 (1986).

22. Snodgrass, F. E. et al. Propagation of ocean swell across the Pacific. *Phil. Trans. R. Soc. Lond. A* **259,** 431–497 (1966).

23. Fairall, C. W. et al. Cool-skin and warm-layer effects on sea surface temperature. *J. Geophys. Res.* **101,** 1295–1308 (1996).

24. Kawai, Y. & Wada, A. Diurnal sea surface temperature variation and its impact on the atmosphere and ocean: a review. *J. Oceanogr.* **63,** 721–744 (2007).

25. Gentemann, C. L. & Minnett, P. J. Radiometric measurements of ocean surface thermal variability. *J. Geophys. Res.* **113,** C08017; https://doi.org/10.1029/2007JC004540 (2008).

26. Watada, S. et al. Atmospheric pressure change associated with the 2003 Tokachi-Oki earthquake. *Geophys. Res. Lett.* **33,** L24306; https://doi.org/10.1029/2006GL027967 (2006).

27. Mikumo, T. et al. Low-frequency acoustic-gravity waves from coseismic vertical deformation associated with the 2004 Sumatra-Andaman earthquake (M_w = 9.2). *J. Geophys. Res.* **113,** B12402; https://doi.org/10.1029/2008JB005710 (2008).

28. Arai, N. et al. Atmospheric boundary waves excited by the tsunami generation related to the 2011 great Tohoku-Oki earthquake. *Geophys. Res. Lett.* **38,** L00G18; https://doi.org/10.1029/2011GL049146 (2011).

29. Ishii, H. & Asai, Y. Characteristics of the stress and barometric seismograms produced by the 2011 Tohoku earthquake (M9.0) and vertical movements derived from barometric seismograms. *Earth Planets Space* **68,** 61; https://doi.org/10.1186/s40623-016-0434-0 (2016).

30. Elipot, S., Lumpkin, R. & Prieto, G. Modification of inertial oscillations by the mesoscale eddy field. *J. Geophys. Res.* **115,** C09010; https://doi.org/10.1029/2009JC005679 (2010).

31. Sun, T. & Davis, E. E. Monitoring the 2021 M_w 8.2 Alaska earthquake by an offshore seismic and fluid pressure observation network and implications for ocean-crust dynamic coupling. *Geochem. Geophys. Geosyst.* **23,** e2022GC010540; https://doi.org/10.1029/2022GC010540 (2022).

32. U.S. Geological Survey. ShakeMap, M 8.8 – 2025 Kamchatka Peninsula, Russia Earthquake (event us6000qw60; version 18, processed 1 October 2026). https://earthquake.usgs.gov/earthquakes/eventpage/us6000qw60/shakemap; product file https://earthquake.usgs.gov/product/shakemap/us6000qw60/us/1790886622188/download/info.json (2025).

33. Ambraseys, N. N. A damaging seaquake. *Earthq. Eng. Struct. Dyn.* **13,** 421–424 (1985).

34. Foster, J. H., Brooks, B. A., Wang, D., Carter, G. S. & Merrifield, M. A. Improving tsunami warning using commercial ships. *Geophys. Res. Lett.* **39,** L09603; https://doi.org/10.1029/2012GL051367 (2012).

35. Inazu, D., Waseda, T., Hibiya, T. & Ohta, Y. Assessment of GNSS-based height data of multiple ships for measuring and forecasting great tsunamis. *Geosci. Lett.* **3,** 25; https://doi.org/10.1186/s40562-016-0059-y (2016).

36. Bernard, E. N. & Titov, V. V. Evolution of tsunami warning systems and products. *Phil. Trans. R. Soc. A* **373,** 20140371; https://doi.org/10.1098/rsta.2014.0371 (2015).

37. Percival, D. B. et al. Extraction of tsunami source coefficients via inversion of DART buoy data. *Nat. Hazards* **58,** 567–590 (2011).

38. Raghukumar, K. et al. Performance characteristics of "Spotter," a newly developed real-time wave measurement buoy. *J. Atmos. Ocean. Technol.* **36,** 1127–1141 (2019).

39. Nosov, M. A. & Kolesov, S. V. Elastic oscillations of water column in the 2003 Tokachi-oki tsunami source: in-situ measurements and 3-D numerical modelling. *Nat. Hazards Earth Syst. Sci.* **7,** 243–249 (2007).

40. Levin, B. W. & Nosov, M. A. *Physics of Tsunamis* 2nd edn (Springer, 2016).

41. Sofar Ocean. (GET) Historical Data. *Spotter Data* https://docs.sofarocean.com/spotter-and-smart-mooring/spotter-data/wave-data (accessed 13 October 2026).

42. Voermans, J. J., Smit, P. B., Janssen, T. T. & Babanin, A. V. Estimating wind speed and direction using wave spectra. *J. Geophys. Res. Oceans* **125,** e2019JC015717; https://doi.org/10.1029/2019JC015717 (2020).

43. U.S. Geological Survey. Advanced National Seismic System (ANSS) Comprehensive Catalog. https://doi.org/10.5066/F7MS3QZH (2017).

44. U.S. Geological Survey. Finite fault model, us6000qw60 (model 1, version 5). https://earthquake.usgs.gov/product/finite-fault/us6000qw60_1/us/1763589364802/properties.json (2025).

45. Liu, C. et al. Simple unilateral rupture of the great M_w 8.8 2025 Kamchatka earthquake. *Science* **391,** 812–817 (2026).

46. Ryan, W. B. F. et al. Global Multi-Resolution Topography synthesis. *Geochem. Geophys. Geosyst.* **10,** Q03014; https://doi.org/10.1029/2008GC002332 (2009).

47. Okada, Y. Surface deformation due to shear and tensile faults in a half-space. *Bull. Seismol. Soc. Am.* **75,** 1135–1154 (1985).

48. Kajiura, K. The leading wave of a tsunami. *Bull. Earthq. Res. Inst. Univ. Tokyo* **41,** 535–571 (1963).

49. Tanioka, Y. & Satake, K. Tsunami generation by horizontal displacement of ocean bottom. *Geophys. Res. Lett.* **23,** 861–864 (1996).

50. NOAA National Data Buoy Center. Water column height (tsunami) (DART®) historical data for 2025, stations 21416, 21419, 21415 and 21414. https://www.ndbc.noaa.gov/data/historical/dart/21416t2025.txt.gz; likewise 21419t2025.txt.gz, 21415t2025.txt.gz and 21414t2025.txt.gz (accessed 11 October 2026).

51. Künsch, H. R. The jackknife and the bootstrap for general stationary observations. *Ann. Stat.* **17,** 1217–1241 (1989).

52. Westfall, P. H. & Young, S. S. *Resampling-Based Multiple Testing: Examples and Methods for p-Value Adjustment* (Wiley, 1993).

53. Benjamini, Y. & Hochberg, Y. Controlling the false discovery rate: a practical and powerful approach to multiple testing. *J. R. Stat. Soc. Ser. B Methodol.* **57,** 289–300 (1995).

54. Wilks, D. S. "The stippling shows statistically significant grid points": how research results are routinely overstated and overinterpreted, and what to do about it. *Bull. Am. Meteorol. Soc.* **97,** 2263–2273 (2016).

55. Heard, N. A. & Rubin-Delanchy, P. Choosing between methods of combining p-values. *Biometrika* **105,** 239–246 (2018).

56. Large, W. G. & Pond, S. Open ocean momentum flux measurements in moderate to strong winds. *J. Phys. Oceanogr.* **11,** 324–336 (1981).

57. Alford, M. H., MacKinnon, J. A., Simmons, H. L. & Nash, J. D. Near-inertial internal gravity waves in the ocean. *Annu. Rev. Mar. Sci.* **8,** 95–123 (2016).

58. Donelan, M. A. & Pierson, W. J. The sampling variability of estimates of spectra of wind-generated gravity waves. *J. Geophys. Res.* **88,** 4381–4392 (1983).

59. Young, I. R. Probability distribution of spectral integrals. *J. Waterw. Port Coast. Ocean Eng.* **112,** 338–341 (1986).

60. Dai, A. & Wang, J. Diurnal and semidiurnal tides in global surface pressure fields. *J. Atmos. Sci.* **56,** 3874–3891 (1999).

61. Copernicus Climate Change Service. ERA5 hourly data on single levels from 1940 to present. *Copernicus Climate Change Service (C3S) Climate Data Store (CDS)* https://doi.org/10.24381/cds.adbb2d47 (2018).

62. Hersbach, H. et al. The ERA5 global reanalysis. *Q. J. R. Meteorol. Soc.* **146,** 1999–2049 (2020).

63. Zippenfenig, P. Open-Meteo.com Weather API. *Zenodo* https://doi.org/10.5281/zenodo.7970649 (2023).

64. Japan Aerospace Exploration Agency. JAXA Himawari Monitor: user's guide (P-Tree System). *Earth Observation Research Center* https://www.eorc.jaxa.jp/ptree/userguide.html (accessed 11 October 2026).

65. NOAA National Data Buoy Center. Station 21416 - Kamchatka Peninsula - 240NM SE of Kamchatka Peninsula, RU. https://www.ndbc.noaa.gov/station_page.php?station=21416 (accessed 11 October 2026).

66. Natural Earth. Free vector and raster map data at 1:10m, 1:50m, and 1:110m scales. https://www.naturalearthdata.com (accessed 11 October 2026).
67. Kletetschka, G. & Maio, C. Code, intermediate results and out-of-sample protocol for "A free-drifting wave buoy above the 2025 M_w 8.8 Kamchatka rupture" (version 1.0). *Zenodo* https://doi.org/10.5281/zenodo.23651939 (2026).
68. Hunter, J. D. Matplotlib: a 2D graphics environment. *Comput. Sci. Eng.* **9,** 90–95 (2007).

Acknowledgements

We thank the community of Native Village Mekoryuk, City of Mekoryuk, Nunivak Island, for making this deployment possible, and Sofar Ocean for keeping the buoy's data publicly accessible. Samson Weston and Bessie Weston for supporting the deployment of the wave buoy and providing their expertise and Indigenous Knowledge of the area. Research product of Short Wave Radiation (produced from Himawari-9) that was used in this paper was supplied by the P-Tree System, Japan Aerospace Exploration Agency (JAXA).

Funding

GK was supported by the Ministry of Education, Youth and Sport of the Czech Republic (Project No. LUAUS25082). CM was supported by National Science Foundation (2318375 and 2220559).

Author contributions

GK wrote the manuscript. CM was responsible for all field work around the deployment of the wave buoy and collection and archival of data as well as edited, reviewed, and approved of the manuscript.

Additional information

Competing interests: The authors declare no competing interests

Supplementary information: Supplementary Information (one PDF: Supplementary Methods S1.1–S1.16, Supplementary Notes S2.1–S2.8, Supplementary Tables S1–S12 and Supplementary Figs. S1–S12) and Supplementary Data S1 (XLSX; derived data tables) accompany this paper.

Correspondence and requests for materials should be addressed to G.K.

Supplementary Files

This is a list of supplementary files associated with this preprint. Click to download.

- SupplementaryInformation.docx